

 Open access • Posted Content • DOI:10.1101/2020.04.01.019646

## **A Pan-Cancer Blueprint of the Heterogeneous Tumour Microenvironment Revealed by Single-Cell Profiling** — [Source link](#)

Junbin Qian, Siel Olbrecht, Bram Boeckx, Hanne Vos ...+20 more authors

**Institutions:** Katholieke Universiteit Leuven, Vrije Universiteit Brussel

**Published on:** 02 Apr 2020 - bioRxiv (Cold Spring Harbor Laboratory)

**Topics:** Stromal cell, Cancer cell, Cell type and Population

Related papers:

- [A pan-cancer blueprint of the heterogeneous tumor microenvironment revealed by single-cell profiling.](#)
- [Phenotype molding of stromal cells in the lung tumor microenvironment.](#)
- [Single-Cell Map of Diverse Immune Phenotypes in the Breast Tumor Microenvironment.](#)
- [Comprehensive Integration of Single-Cell Data.](#)
- [Dissecting the multicellular ecosystem of metastatic melanoma by single-cell RNA-seq](#)

Share this paper:    

View more about this paper here: <https://typeset.io/papers/a-pan-cancer-blueprint-of-the-heterogeneous-tumour-h9maeqndep>

# A PAN-CANCER BLUEPRINT OF THE HETEROGENEOUS TUMOUR MICROENVIRONMENT REVEALED BY SINGLE-CELL PROFILING

Running title: Pan-cancer heterogeneity of stromal cells

## AUTHORS:

Junbin Qian<sup>1,2</sup>, Siel Olbrecht<sup>1,2,3</sup>, Bram Boeckx<sup>1,2</sup>, Hanne Vos<sup>4</sup>, Damya Laoui<sup>5,6</sup>, Emre Etlioglu<sup>7</sup>, Els Wauters<sup>8,9</sup>, Valentina Pomella<sup>7</sup>, Sara Verbandt<sup>7</sup>, Pieter Busschaert<sup>3</sup>, Ayse Bassez<sup>1,2</sup>, Amelie Franken<sup>1,2</sup>, Marlies Vanden Bempt<sup>1,2</sup>, Jieyi Xiong<sup>1,2</sup>, Birgit Weynand<sup>10</sup>, Yannick van Herck<sup>11</sup>, Asier Antoranz<sup>10</sup>, Francesca Maria Bosisio<sup>10</sup>, Bernard Thienpont<sup>12</sup>, Giuseppe Floris<sup>10</sup>, Ignace Vergote<sup>3</sup>, Ann Smeets<sup>4</sup>, Sabine Tejpar<sup>7</sup>, Diether Lambrechts<sup>1,2,\*</sup>

## AFFILIATIONS:

<sup>1</sup> VIB Center for Cancer Biology, Leuven, Belgium

<sup>2</sup> Laboratory for Translational Genetics, Department of Human Genetics, KU Leuven, Leuven, Belgium

<sup>3</sup> Department of Obstetrics and Gynaecology, University Hospitals Leuven, Leuven, Belgium

<sup>4</sup> Department of Oncology, KU Leuven, Surgical Oncology, University Hospitals Leuven, Leuven, Belgium

<sup>5</sup> Laboratory of Cellular and Molecular Immunology, Vrije Universiteit Brussel, Brussels, Belgium

<sup>6</sup> Laboratory of Myeloid Cell Immunology, VIB Center for Inflammation Research, Brussels, Belgium

<sup>7</sup> Laboratory of Molecular Digestive Oncology, Department of Oncology, KU Leuven, Leuven, Belgium

<sup>8</sup> Respiratory Oncology Unit (Pneumology) and Leuven Lung Cancer Group, University Hospital KU Leuven, Leuven, Belgium

<sup>9</sup> Laboratory of Pneumology, Department of Chronic Diseases, Metabolism and Ageing, KU Leuven, Leuven, Belgium

<sup>10</sup> Laboratory of Translational Cell & Tissue Research, Department of Imaging and Pathology, University Hospitals Leuven, KU Leuven, Leuven, Belgium

<sup>11</sup> Laboratory of Experimental Oncology, KU Leuven, Leuven, Belgium

<sup>12</sup> Laboratory for Functional Epigenetics, Department of Human Genetics, KU Leuven, Leuven, Belgium

\*Correspondence: Diether.Lambrechts@kuleuven.vib.be

40 **ABSTRACT**

41 The stromal compartment of the tumour microenvironment consists of a heterogeneous  
42 set of tissue-resident and tumour-infiltrating cells, which are profoundly moulded by  
43 cancer cells. An outstanding question is to what extent this heterogeneity is similar  
44 between cancers affecting different organs. Here, we profile 233,591 single cells from  
45 patients with lung, colorectal, ovary and breast cancer (n=36) and construct a pan-  
46 cancer blueprint of stromal cell heterogeneity using different single-cell RNA and protein-  
47 based technologies. We identify 68 stromal cell populations, of which 46 are shared  
48 between cancer types and 22 are unique. We also characterise each population  
49 phenotypically by highlighting its marker genes, transcription factors, metabolic activities  
50 and tissue-specific expression differences. Resident cell types are characterised by  
51 substantial tissue specificity, while tumour-infiltrating cell types are largely shared across  
52 cancer types. Finally, by applying the blueprint to melanoma tumours treated with  
53 checkpoint immunotherapy and identifying a naïve CD4<sup>+</sup> T-cell phenotype predictive of  
54 response to checkpoint immunotherapy, we illustrate how it can serve as a guide to  
55 interpret scRNA-seq data. In conclusion, by providing a comprehensive blueprint  
56 through an interactive web server, we generate a first panoramic view on the shared  
57 complexity of stromal cells in different cancers.

58

59

60

61

62

63

64

65

66

67

68

69 **KEYWORDS**

70 Tumour microenvironment; stromal cell heterogeneity; single-cell RNA-seq; CITE-  
71 seq; therapeutic target; clinical response

## 72 INTRODUCTION

73 In recent years, single-cell RNA sequencing (scRNA-seq) studies have provided an  
74 unprecedented view on how stromal cells consist of heterogeneous and phenotypically  
75 diverse populations of cells. Indeed, by now, the tumour microenvironment (TME) of  
76 several cancer types has been profiled, including melanoma<sup>1</sup>, lung cancer<sup>2</sup>, head and neck  
77 cancer<sup>3</sup>, hepatocellular carcinoma<sup>4</sup>, glioma<sup>5</sup>, medulloblastoma<sup>6</sup>, pancreatic cancer<sup>7</sup>, *etc.*  
78 However, while there is still an unmet need to chart TME heterogeneity in additional  
79 tumours and cancer types, the higher-level question relates to the similarities between  
80 these microenvironments.

81 Indeed, it remains unexplored whether the same stromal cell phenotypes are present in  
82 different cancer types. Also, it is not clear to what extent these phenotypes are reminiscent  
83 of the normal tissue from which they originate and are thus characterised by tissue-  
84 specific expression. Such knowledge is highly desirable, because it not only facilitates  
85 comparison between different scRNA-seq studies, but also contributes to our insights in  
86 cancer type-specific gene expression patterns and treatment vulnerabilities.

87 Furthermore, this knowledge would allow us to assess at single-cell level the underlying  
88 mechanisms of action of novel cancer therapies. Indeed, most innovative cancer therapies  
89 are given to cancer patients with advanced disease, in which tissue biopsies often can  
90 only be collected from metastasized organs. It is difficult, however, to systematically  
91 identify stromal phenotypes in biopsies taken from different organs, as their expression is  
92 determined by the metastasized tissue. Another challenge is that rare stromal cell  
93 phenotypes often cluster together with other more common phenotypes, and can  
94 therefore only be detected when several 10,000s of cells derived from multiple patient  
95 biopsies are profiled together. Many of these rare phenotypes are critical in determining  
96 response to cancer treatment and therefore need to be assessed as a separate population  
97 of cells. For instance, scRNA-seq of melanoma T-cells exposed to anti-PD1 identified  
98 TCF7<sup>+</sup> CD8<sup>+</sup> memory-precursor T-cells as the population underlying treatment response.  
99 These cells are rare, as they represent only ~15% of CD8<sup>+</sup> T-cells, which by themselves  
100 represent only ~2.5% of cells in these tumours<sup>8</sup>. In order not to miss these rare  
101 phenotypes, a blueprint of the different cell populations present in each cancer type would  
102 be of considerable benefit.

103 We therefore generated a comprehensive blueprint of stromal cell heterogeneity across  
104 cancer types and provide a detailed view on the shared complexity and heterogeneity of  
105 stromal cells in these cancers. We illustrate how this blueprint can serve as a guide to  
106 interpret scRNA-seq data at individual patient level, even when comparing tumours  
107 collected from different tissues or profiled using different scRNA-seq technologies. Our  
108 single-cell blueprint can be visualised, analysed and downloaded from an interactive web  
109 server (<http://blueprint.lambrechtslab.org>).

## 110 **RESULTS**

### 111 ***scRNA-seq and cell typing of tumour and normal tissue***

112 First, we performed scRNA-seq on tumours from 3 different organs (or cancer types):  
113 colorectal cancer (CRC, n=7), lung cancer (LC, n=8) and ovarian cancer (OvC, n=5).  
114 Whenever possible, we retrieved both malignant (tumour) and matched non-malignant  
115 (normal) tissue during surgical resection with curative intent. All tumours were treatment-  
116 naïve and reflected different disease stages (e.g. stage I-IV CRC) or histopathologies (e.g.  
117 adenocarcinoma versus squamous LC), and whenever possible tissues were collected  
118 from different anatomic sites (e.g. primary tumour from the ovary and omentum in OvC,  
119 or from core *versus* border regions in CRC). Overall, 50 tumour tissues and 17 normal  
120 tissues were profiled (**Fig. 1a**). Clinical and tumour mutation data are summarised in  
121 **Tables S1-3**.

122 Following resection, tissues were rapidly digested to a single-cell suspension and  
123 unbiasedly subjected to 3'-scRNA-seq. After quality filtering (Methods), we obtained ~1  
124 billion unique transcripts from 183,373 cells with >200 genes detected. Of these, 71.7%  
125 of cells originated from malignant tissue. Principle component analysis (PCA) using  
126 variably expressed genes was used to generate t-SNEs at different resolutions  
127 (Supplementary information, **Fig. S1a,b**). Marker genes were used to identify cell types  
128 (Supplementary information, **Fig. S1c**). At low resolution, cells clustered based on cancer  
129 type, whereas at high resolution they clustered based on patient identity (Supplementary  
130 information, **Fig. S1d**). Also, when assessing how cell types previously identified in LC  
131 now clustered<sup>2</sup>, obvious differences were noted, with similar phenotypic cells now  
132 belonging to distinct clusters.

133

### 134 **Sub-phenotyping of cell types**

135 We therefore used a different strategy. First, we clustered cells for each cancer type  
136 separately and assigned cell type identities to each cell (**Fig. 1a**). This revealed that cells  
137 mostly clustered based on cell type (**Fig. 1b** and Supplementary information, **Fig. S1e**),  
138 allowing us to assess the relative contribution of tumour *versus* normal tissue or individual  
139 patients to each cell type (**Fig. 1c-e**, and Supplementary information, **Fig. S1f**). We  
140 observed that dendritic cells were transcriptionally most active, while T-cells were the  
141 most frequent cell type across cancer types (**Fig. 1e-f**), especially in LC (as observed in  
142 other datasets; Supplementary information, **Fig. S1g**). We also identified cell types  
143 specific for one cancer type, including lung alveolar, epithelial and enteric glial cells.

144 Next, we pooled cells from different cancer types based on cell type identity and  
145 performed PCA-based unaligned clustering, generating t-SNEs displaying the phenotypic  
146 heterogeneity for each cell type (**Fig. 1a**). For alveolar, epithelial and enteric glial cells this  
147 generated 15 tissue-specific subclusters (LC: 5 alveolar clusters and 1 epithelial cluster;  
148 CRC: 8 epithelial clusters and 1 enteric glial cluster), most of which have been described  
149 previously<sup>9,10</sup> (Supplementary information, **Fig. S1h-p**). Additionally, 7 tissue-specific  
150 subclusters were identified amongst the fibroblasts and macrophages (see below).  
151 Separately, we performed canonical correlation analysis (CCA) for each cancer type  
152 followed by graph-based clustering to generate a t-SNE per cell type (**Fig. 1a**)<sup>11</sup>. To avoid  
153 that CCA would erroneously assign cells unique for a cancer type, we did not include any  
154 of the 22 tissue-specific subclusters. Thus, while unaligned clustering revealed patient or  
155 cancer type-specific clusters, CCA aligned common sources of variation between cancer  
156 types. Two measures to calculate sample bias (i.e., ‘Shannon index’ and ‘mixing metrics’,  
157 see Methods) confirmed that after CCA bias decreased in all clusters (Supplementary  
158 information, **Fig. S1q,r**).

159 Overall, we identified 68 stromal subclusters or phenotypes, of which 46 were shared  
160 across cancer types. The number of phenotypes varied between cell types, ranging  
161 between 5 to 11 for dendritic cells and fibroblasts, respectively. Our approach was less  
162 successful for cancer cells, which due to underlying genetic heterogeneity continued to  
163 cluster patient-specifically (Supplementary information, **Fig. S1s-u**). The number of  
164 cancer cells varied substantially between tumours, while also T-cells, myeloid cells and  
165 B-cells varied considerably (Supplementary information, **Fig. S1v,w**).

166 Below, we describe each stromal phenotype in more detail, highlighting the number of  
167 cells, read counts and transcripts across all cancer types and for each cancer type  
168 separately, both in tumour *versus* normal tissue (**Table S4**). Additionally, marker genes  
169 and functional characteristics of each phenotype are highlighted (**Table S5**). The  
170 enrichment or depletion of these phenotypes in a cancer type (LC, CRC and OvC) or tissue  
171 (tumour *versus* normal) are evaluated (**Table S6**), while gene set enrichment analysis for  
172 biological and disease pathways (REACTOME and Gene Ontology) is also performed (see  
173 <http://blueprint.lambrechtslab.org>).

#### 174 ***Endothelial cells, tissue-specificity confined to normal tissue***

175 Clustering the transcriptomes of 8,223 endothelial cells (ECs) using unaligned and CCA-  
176 aligned approaches identified, respectively, 13 and 9 clusters, each with corresponding  
177 marker genes (**Fig. 2a-c** and Supplementary information, **Fig. S2a-c**). Five CCA-aligned  
178 clusters were shared between cancer types (**Fig. 2d,e**), including, based on marker gene  
179 expression, C1\_ESM1 tip cells (*ESM1*, *NID2*), C2\_ACKR1 high endothelial venules (HEVs)  
180 and venous ECs (*ACKR1*, *SELP*), C3\_CA4 capillary (*CA4*, *CD36*), C4\_FBLN5 arterial  
181 (*FBLN5*, *GJA5*) and C5\_PROX1 lymphatic (*PROX1*, *PDPN*) ECs. Three other clusters  
182 displayed T-cell (C6\_CD3D), pericyte (C7\_RGS5) and myeloid-specific (C8\_AIF1) marker  
183 genes and consisted of doublet cells, while one cluster consisted of low-quality ECs (C9;  
184 Supplementary information, **Fig. S2d,e**). Tip ECs only resided in malignant tissue and were  
185 most prevalent in CRC, while also HEVs were enriched in tumours. In contrast, capillary  
186 ECs (cECs) were enriched in normal tissue (**Fig. 2d-f**; Supplementary information, **Fig.**  
187 **S2f**). We identified several genes differentially expressed between tumour and normal  
188 tissue (Supplementary information, **Fig. S2g** and **Table S7**). For instance, the pro-  
189 angiogenic factor perlecan (or *HSPG2*) was highly expressed in tumour *versus* normal  
190 cECs.

191 There were 5 unaligned cEC clusters, which clustered together (in C3\_CA4) after CCA.  
192 Among these, 4 were derived from normal tissue (NEC1-4; **Fig. 2g**). Moreover, NEC1-3s  
193 were all from lung, suggesting that most cEC heterogeneity is ascribable to normal lung.  
194 C3\_NEC1s represented alveolar cECs based on the absence of *VWF*, while C3\_NEC2s  
195 and C3\_NEC3s represented extra-alveolar cECs (**Fig. 2g-i**)<sup>12,13</sup>. C3\_NEC1s expressed  
196 *EDNRB*, an oxygen-sensitive regulator mediating vasodilation<sup>14</sup>, but also IL33-receptor

197 *IL1RL1* (ST2). This is surprising as major IL-33 effector cell types are thus far only immune  
198 cells, including basophils and innate lymphocytes<sup>10</sup>. Both extra-alveolar cNEC clusters  
199 expressed *EDN1*, which is a potent vasoconstrictor. C3\_NEC3s additionally expressed  
200 cytokines, chemotactic and immune cell homing molecules (e.g. *IL6*, *CCL2*, *ICAM1*)  
201 (Supplementary information, **Fig. S2h**). In contrast, C3\_NEC4s were exclusively  
202 composed of ovary and colon-derived cells, suggesting similarities between NECs from  
203 both tissues. A polarized distribution of ovary and colon-derived ECs within the C3\_NEC4  
204 cluster (**Fig. 2g**) suggests, however, that there are also differences between both tissues.  
205 In contrast, tumour cECs (C3\_TECs) were derived from all 3 cancer types and lacked  
206 tissue specificity on the t-SNE. Indeed, C3\_TECs were all characterised by tumour EC  
207 markers *PLVAP* and *IGFBP7*<sup>15-17</sup> (Supplementary information, **Fig. S2h, Table S5**), and  
208 only few genes were differentially expressed between cancer types in TECs  
209 (Supplementary information, **Fig. S2i**).

210 SCENIC<sup>18</sup> identified different transcription factors (TFs) underlying each EC phenotype  
211 (**Fig. 2j-k** and Supplementary information, **Table S8**). For instance, activation of NF- $\kappa$ B  
212 (NFKB1) and HOXB pathways was confined to C3\_NEC3s and C3\_TECs, respectively.  
213 Metabolic pathway analysis revealed distinct metabolic signatures among EC phenotypes  
214 (**Fig. 2l,m**): glycolysis and oxidative phosphorylation, which promote vessel sprouting<sup>19</sup>,  
215 were upregulated in tip cells, while fatty acid oxidation, essential for lymphangiogenesis  
216 was increased in lymphatic ECs<sup>19</sup>. Metabolic activities within cECs also differed: carbonic  
217 acid metabolism was most active in C3\_NEC1, confirming these are alveolar cECs, which  
218 actively convert carbonic acid into CO<sub>2</sub> during respiration. However, carbonic acid  
219 metabolism was reduced in C3\_TECs, which instead deployed glycolysis and oxidative  
220 phosphorylation (Supplementary information, **Fig. S2j**). Similar characteristics were  
221 observed when assessing activation of cancer hallmark pathways (Supplementary  
222 information, **Fig. S2k,l**).

### 223 ***Fibroblasts show the highest cancer type specificity***

224 Fibroblasts are highly versatile cell types endowed with extensive heterogeneity<sup>20</sup>. Indeed,  
225 unaligned clustering of 24,622 fibroblasts resulted in 17 clusters (**Fig. 3a,b**), which were  
226 often tissue-specific (Supplementary information, **Fig. S3a-d**). Particularly, C1-C3  
227 represented colon-specific clusters derived from normal tissue, while C4-C6 represented



228 stroma (C4, C5) and mesothelium-derived cells (C6) specific for the ovary. C1-C6  
229 fibroblasts were excluded from CCA, because they have a tissue-specific identity,  
230 localization and function that are unlikely to have counterparts in other tissues (see below).  
231 All other fibroblasts clustered into 5 clusters shared across cancer types and patients (C7-  
232 C11; **Fig. 3c-e** and Supplementary information, **Fig. S3e**). Three other CCA clusters  
233 represented a low-quality (C12) or doublet cluster (C13\_CD3D, C14\_AIF1) (Supplementary  
234 information, **S3f,g**). Fibroblasts therefore consist of 11 cellular phenotypes: tissue-specific  
235 clusters C1-C6 identified by unaligned clustering and shared clusters C7-C11 identified  
236 by CCA (**Fig. 3f,g** for marker genes and functional gene sets).

237 Colon-specific C1-C3s mostly resided in normal tissue (**Fig. 3e**). C1\_KCNN3 fibroblasts  
238 co-expressed *KCNN3* and *P2RY1* (**Fig. 3f**), a potassium calcium-activated channel (SK3-  
239 type) and purine receptor (*P2Y1*), respectively. Their co-expression defines a novel  
240 excitable cell that co-localizes with motor neurons in the gastrointestinal tract and  
241 regulates their purinergic inhibitory response to smooth muscle function in the colon<sup>21,22</sup>.  
242 C1\_KCNN3s also expressed *LY6H*, a neuron-specific regulator of nicotine-induced  
243 glutamatergic signalling<sup>23</sup>, suggesting these cells to regulate multiple neuromuscular  
244 transmission processes. C2\_ADAMDEC1s represented mesenchymal cells of the colon  
245 lamina propria<sup>24</sup>, characterised by *ADAMDEC1* and *APOE*. C3\_SOX6s were marked by  
246 *SOX6* expression, as well as *BMP4*, *BMP5*, *WNT5A* and *FRZB* expression (**Fig. 3f**).  
247 They are located in close proximity to the epithelial stem cell niche and promote stem cell  
248 maintenance in the colon<sup>24</sup>. C4-C5 ovarian stroma cells were marked by *STAR* and  
249 *FOXL2*<sup>25,26</sup>, which promote folliculogenesis<sup>27</sup>. Both clusters also expressed *DLK1*, which  
250 is typical for embryonic fibroblasts. C4\_STARs were derived from normal tissue, while  
251 C5\_STARs were exclusive to tumour tissue, suggesting that C4\_STARs give rise to  
252 C5\_STARs<sup>25</sup>. Based on calretinin (*CALB2*) and mesothelin (*MSLN*) expression,  
253 C6\_CALB2s were likely to represent mesothelium-derived cells<sup>28</sup>. These cells were  
254 especially enriched in omentum (Supplementary information, **Fig. S3h**), known to contain  
255 numerous mesothelial cells.

256 C7\_MYH11 corresponded to myofibroblasts and were characterised by high expression  
257 of smooth muscle-related contractile genes, including *MYH11*, *PLN* and *ACTG2* (**Fig. 3f**).  
258 C8\_RGS5 represented pericytes (*RGS5*, *PDGFRB*), which similar as myofibroblasts  
259 expressed contractile genes, but also showed pronounced expression of RAS superfamily

260 members (*RRAS*, *RASL12*). Additionally, pericytes expressed a distinct subset of  
261 collagens (*COL4A1*, *COL4A2*, *COL18A1*), genes involved in angiogenesis (*EGFL6*,  
262 *ANGPT2*; **Fig. 3g**) and vessel maturation (*NID1*, *LAMA4*, *NOTCH3*; Supplementary  
263 information, **Fig. S3i**). Pericytes were enriched in malignant tissue (**Fig. 3e,h** and  
264 Supplementary information, **Fig. S3j**). When comparing pericytes from malignant *versus*  
265 normal tissue, the former exhibited increased expression of collagens and angiogenic  
266 factors (*PDGFA*, *VEGFA*; Supplementary information, **Fig. S3k**), but reduced expression  
267 of the vascular stabilization factor *TIMP3*<sup>29</sup>. These differences may contribute to a leaky  
268 tumour vasculature. C9\_CFDs expressed adipocyte markers adipisin (*CFD*) and  
269 apolipoprotein D (*APOD*), suggesting these are adipogenic fibroblasts. They are positively  
270 associated with aging in the dermis<sup>30</sup>, but their role in malignancy has not been  
271 established. Notably, in the unaligned clusters, C9s separated into 3 tissue-specific  
272 clusters and a single cancer-associated fibroblasts (CAF) cluster (**Fig. 3a**), suggesting that  
273 C9 fibroblasts (similar as cECs) lose tissue-specificity in the TME.

274 C10-C11 represented CAFs showing strong activation of cancer hallmark pathways,  
275 including glycolysis, hypoxia, and epithelial-to-mesenchymal transition (Supplementary  
276 information, **Fig. S3l**). C10\_COMPs typically expressed metalloproteinases (MMPs),  
277 TGF $\beta$ -signalling molecules and extracellular matrix (ECM) genes, including collagens (**Fig.**  
278 **3g**). They also expressed the TGF- $\beta$  co-activator *COMP*, which is activated during  
279 chondrocyte differentiation, and activin (*INHBA*), which synergizes with TGF- $\beta$   
280 signalling<sup>31,32</sup>. Accordingly, chondrocyte-specific TGF- $\beta$  targets (*COL10A1*, *COL11A1*)  
281 were strongly upregulated. C11\_SERPINE1s exhibited increased expression of *SERPINE1*,  
282 *IGF1*, *WT1* and *CLDN1*, which all promote cell migration and/or wound healing via various  
283 mechanisms<sup>33-36</sup>. They also expressed collagens, albeit to a lesser extent as C10\_COMPs.  
284 Additionally, high expression of the pro-angiogenic *EGFL6* suggests these cells to exert  
285 paracrine functions<sup>37,38</sup>. Interestingly, the number of C10-C11 CAFs correlated positively  
286 with the presence of cancer cells (Supplementary information, **Fig. S3m**), confirming the  
287 role of CAFs in promoting tumour growth<sup>20</sup>.

288 Using SCENIC, we identified TFs unique to each fibroblast cluster (**Fig. 3i**). For instance,  
289 MYC and EGR3 underpinned C11\_CAFs, while pericytes were characterised by EPAS1,  
290 TBX2 and NR2F2 activity. Interestingly, MYC activation of CAFs promote aggressive  
291 features of cancers through upregulation of unshielded RNA in exosome<sup>39</sup>. At the

292 metabolic level, we observed that creatine and cyclic nucleotide metabolism, which are  
293 essential for smooth muscle function, were upregulated in myofibroblasts (C7), while  
294 glycolysis was most prominent in C10-11 CAFs (**Fig. 3j**). Indeed, highly proliferative CAFs  
295 rely on aerobic glycolysis, and their glycolytic adaptation promote a reciprocal metabolic  
296 symbiosis between CAFs and cancer cells<sup>20</sup>.

### 297 ***Dendritic cells, novel markers of cDC maturation revealed***

298 Clustering the transcriptomes of 2,722 DCs identified 5 different DC phenotypes using  
299 unaligned and CCA-aligned approaches (**Fig. 4a**). 92% of cells clustered similarly with  
300 both approaches, suggesting DCs in line with their non-resident nature to have limited  
301 cancer type specificity. C1\_CLEC9As corresponded to conventional DCs type 1 (cDC1;  
302 *CLEC9A*, *XCR1*)<sup>40,41</sup>, C2\_CLEC10As to cDCs type 2 (cDC2; *CD1C*, *CLEC10A*, *SIRPA*),  
303 while C3\_CCR7s represented migratory cDCs (*CCR7*, *CCL17*, *CCL19*; **Fig. 4b,c** and  
304 Supplementary information, **Fig. S4a,b**). Further, C4\_LILRA4s represented plasmacytoid  
305 DCs (pDCs; *LILRA4*, *CXCR3*, *IRF7*), while C5\_CD207s were related to cDC2s based on  
306 *CD1C* expression. C5\_CD207s additionally expressed Langerhans cell-specific markers:  
307 *CD207* (langerin) and *CD1A*, but not the epithelial markers *CDH1* and *EPCAM*, typically  
308 expressed in Langerhans cells<sup>42</sup>. These cells therefore likely represent a subset of cDC2s  
309 with a similar expression as Langerhans cells. Notably, Langerhans-like and migratory  
310 DCs were not previously characterised by scRNA-seq, possibly because these studies  
311 focused on blood-derived DCs<sup>40</sup>.

312 Overall, C2\_CLEC10As were most abundant, while the number of other DCs varied per  
313 cancer type. For instance, C3 was rare in OvC, and C5 enriched in malignant tissue (**Fig.**  
314 **4d,e** and Supplementary information, **Fig. S4c,d**). SCENIC confirmed known TFs to  
315 underlie each DC phenotype, including *BATF3* for cDC1s, *CEBPB* for cDC2s, *NFKB2* for  
316 migratory cDCs and *TCF4* for pDCs (**Fig. 4f,g**). We also identified novel TFs  
317 (Supplementary information, **Table S8**). For instance, *SPI1*, a master regulator of  
318 Langerhans cell differentiation<sup>43</sup>, and *RXRA*, required for cell survival and antigen  
319 presentation in Langerhans cells<sup>44</sup>, were both expressed in C5. Cancer hallmark pathway  
320 analysis revealed activation of interferon- $\alpha$  and - $\gamma$  signalling in migratory cDCs, while  
321 metabolic pathway analysis confirmed a critical role for folate metabolism (Supplementary  
322 information, **Fig. S4e,f**)<sup>45</sup>.

323 By leveraging trajectory inference analyses (using 3 different pipelines; Methods), we  
324 recapitulated the cDC maturation process and observed that cDC2s are enriched in the  
325 migrating branch (**Fig. 4h,i**), suggesting that migratory cDCs originated from cDC2s but  
326 not cDC1s, at least in tumours. Consistent herewith, some migratory cDC-related genes,  
327 i.e. *CCL17* and *CCL22*, were already upregulated in a subset of cDC2s (Supplementary  
328 information, **Fig. S4g**), highlighting that cDC2s are in a transitional state. In contrast, cDC  
329 maturation markers *CCR7* and *LAMP3* were only upregulated at a later stage of the  
330 trajectory (**Fig. 4j**, Supplementary information, **Fig. S4h**)<sup>46</sup>. Interestingly, in OvC, cDC2s  
331 got stuck early in the differentiation lineage compared to CRC and LC (Supplementary  
332 information, **Fig. S4i**). By modelling expression along the branches, we retrieved 4 clusters  
333 with distinct temporal expression (**Fig. 4k**), in which we identified 30 and 210 genes up-  
334 or down-regulated (Supplementary information, **Table S9**). For example, *CLEC10A* was  
335 gradually lost during cDC2 maturation, while *BIRC3* was upregulated, suggesting they  
336 represent novel markers of cDC maturation. Also, when investigating TF dynamics from  
337 cDC2s to migratory cDCs, we identified 22 up- and 23 down-regulated TFs, respectively  
338 (**Fig. 4l** and Supplementary information, **Fig. S4j**).

### 339 ***B-cells, comprehensive taxonomy and developmental trajectory***

340 Amongst the 15,247 B-cells, we identified 8 clusters using unaligned clustering (**Fig. 5a**)  
341 Three of these represented follicular B-cells (*MS4A1/CD20*), which reside in lymphoid  
342 follicles of intra-tumour tertiary lymphoid structures, while 4 clusters were antibody-  
343 secreting plasma cells (*MZB1* and *SDC1/CD138*) (Supplementary information, **Fig. S5a-**  
344 **b**). We also retrieved a T-cell (*C9\_CD3D*) doublet cluster (Supplementary information, **Fig.**  
345 **S5c**). CCA identified 2 additional clusters: one unaligned follicular B-cell cluster, which  
346 was split into 2 separate clusters (C2 and C3, **Fig. 5a-b**) and one additional cancer cell  
347 (*C10\_KRT8*) doublet cluster (Supplementary information, **S5c**). Overall, this resulted in 8  
348 relevant B-cell clusters, each of them characterised by functional gene sets (**Fig. 5c**).

349 Follicular B-cells were composed of mature-naïve (*CD27<sup>-</sup>*, C1) and memory (*CD27<sup>+</sup>*, C2-  
350 4) B-cells (**Fig. 5c**). The former are characterised by a unique *CD27<sup>-</sup>*  
351 *IIGHD<sup>+</sup>(IgD)/IGHM<sup>+</sup>(IgM)* signature and give rise to the latter by migrating through the  
352 germinal centre (GC; referred to as GC-memory B-cells). This process requires expression  
353 of migratory factors *CCR7* (for GC entry) and *GPR183* (for GC exit; Supplementary

354 information, **Fig. S5d**)<sup>47</sup>. In the GC, *IGHM* undergoes class-switch recombination to form  
355 other immunoglobulin isotypes. Indeed, GC-memory B-cells separated into *IGHM*<sup>+</sup> and  
356 *IGHM*<sup>-</sup> populations, i.e., C2 *IGHM*<sup>+</sup> and C3 *IGHM*<sup>-</sup> clusters (**Fig. 5a-c**). A rare population  
357 of memory B-cells is generated independently of the GC<sup>48</sup>. These GC-independent  
358 memory B-cells corresponded to C4\_CD27<sup>+</sup>/CD38<sup>+</sup>s, lacking GC migratory factors  
359 *GPR183* and *CCR7*, but expressing the anti-GC migration factor *RGS13*, which may form  
360 the basis for their GC exclusion (**Fig. 5b** and Supplementary information, **Fig. S5d**)<sup>49</sup>.  
361 Although little is known about GC-independent B-cells, they appear early during immune  
362 response and respond to a broader range of antigens with less specificity as GC-memory  
363 B-cells<sup>50</sup>. Interestingly, C4s exhibited an expression signature intermediate to mature-  
364 naïve and GC-memory B-cells (Supplementary information, **Fig. S5e**). Expression of *IGHD*  
365 and *IGHM* was low, while *IGHG1* and *IGHG3* were elevated (Supplementary information,  
366 **Fig. S5f**), suggesting C4s to have completed class-switch recombination. Indeed, *AICDA*  
367 expression, which induces mutations in class-switch regions during recombination<sup>50</sup>, was  
368 elevated in C4s (**Fig. 5c**). They were also characterised by several uniquely expressed  
369 genes and enriched for proliferative cells (Supplementary information, **Fig. S5g** and **Table**  
370 **S5**). Next to follicular B-cells, we identified 4 clusters of plasma B-cells (C5-C8), which  
371 can be separated based on expression of immunoglobulin heavy chains, i.e. *IGHG1* (IgG)  
372 versus *IGHA1* (IgA). Both could be further stratified based on their antibody-secreting  
373 capacity as determined by *PRDM1* (Blimp-1)<sup>50</sup>: low versus high for immature versus  
374 mature plasma cells, overall resulting in 4 plasma B-cell clusters (**Fig. 5c**).

375 Importantly, B-cell clusters were enriched in all tumours, except for IgA-expressing  
376 plasma cells, which mainly resided in mucosa-rich normal colon (**Fig. 5d,e** and  
377 Supplementary information, **Fig. S5h-j**). Additionally, GC-independent memory B-cells  
378 were most prevalent in CRC. B-cells were also enriched in border versus core fractions of  
379 LC tumours (Supplementary information, **Fig. S5k**). Using SCENIC, each B-cell cluster  
380 was characterised by a unique set of TFs (**Fig. 5f**). For instance, GC-independent memory  
381 B-cells upregulated NF-κB (RELB) and STAT6, which is known to suppress *GPR183*<sup>51</sup>.  
382 Some TFs were upregulated in mature (*PRDM1*<sup>high</sup>) plasma cells, irrespective of their heavy  
383 chain expression. These included multiple immediate-early response TFs (FOS, JUN and  
384 EGR1) and the interferon regulatory factor IRF1 (Supplementary information, **Fig. S5l**),  
385 suggesting they are involved in plasma cell maturation. C5\_IgG\_mature B-cells, relative

386 to all other plasma B-cells, exhibited strong activation of nearly all cancer hallmark  
387 pathways, indicating an active role of C5s in the TME (Supplementary information, **Fig.**  
388 **S5m**).

389 Trajectory inference analysis confirmed that mature-naïve B-cells differentiate into either  
390 GC-memory IgM<sup>+</sup> or IgM<sup>-</sup> branches. As expected, IgM<sup>+</sup> but not IgM<sup>-</sup> cells were located  
391 halfway the trajectory (**Fig. 5g** and Supplementary information, **Fig. S5n**), confirming IgM<sup>+</sup>  
392 cells to undergo class-switch recombination into IgM<sup>-</sup> cells. Memory B-cells of the IgM<sup>+</sup>  
393 and IgM<sup>-</sup> lineages were similarly distributed in OvC and CRC, but in LC they were more  
394 differentiated (Supplementary information, **Fig. S5o**). By overlaying gene expression  
395 dynamics on the trajectory, we identified several genes up- or down-regulated along the  
396 pseudotime, including *CD27* and *TCL1A*, respectively (**Fig. 5h**; Supplementary  
397 information, **Fig. S5p,q** and **Table S9**). In line with *CCR7* and *GPR183* determining GC  
398 entry and exit, *CCR7* was expressed in mature-naïve B-cells (C1, before entry) but  
399 disappeared in *IGHM*<sup>-</sup> B-cells. *Vice versa*, *GPR183* was only expressed after GC entry (C2  
400 and C3, Supplementary information, **Fig. S5d,q**). Similarly, we assessed the trajectory of  
401 class-switched GC-memory B-cells (C3) differentiating into plasma cells. We confirmed  
402 that GC-memory B-cells differentiate into either IgG<sup>+</sup>- or IgA<sup>+</sup>-expressing plasma cells (**Fig.**  
403 **5i**) and that both branches subsequently dichotomize into mature or immature states  
404 based on *PRDM1* expression (**Fig. 5j**). Cells were similarly distributed along the trajectory  
405 regardless of the cancer type, although in LC there was an enrichment towards the  
406 beginning of the IgA lineage (Supplementary information, **Fig. S5r**). Further, when  
407 assessing underlying expression dynamics along the trajectory, we identified several  
408 genes staging the differentiation process (Supplementary information, **Fig. S5s** and **Table**  
409 **S9**). For example, we found *TNFRSF17* (also known as B-cell maturation antigen) to  
410 increase along the IgA<sup>+</sup> plasma cell trajectory<sup>52</sup>.

#### 411 ***T-/NK-cells show cancer type-dependent prevalence***

412 Altogether, 52,494 T- and natural killer (NK) cells clustered into 12 and 11 clusters using  
413 unaligned and CCA-aligned methods (**Fig. 6a,b**). The additional cluster identified by  
414 unaligned clustering (C12) was composed of cells from normal lung tissue (Supplementary  
415 information, **Fig. S6a,b**). CCA did not affect clustering of T-/NK-cells in tumours,  
416 indicating that T-cells have limited cancer type-specific differences. Besides C12 and a

417 low-quality cluster (C11, Supplementary information, **Fig. S6c,d**), T-/NK-cells consisted  
418 of 10 phenotypes, including 4 CD8<sup>+</sup> T-cell (C1-C4), 4 CD4<sup>+</sup> T-cell (C5-C8) and 2 NK-cell  
419 clusters (C9-C10).

420 The C1\_CD8\_HAVCR2 cluster consisted of exhausted CD8<sup>+</sup> cytotoxic T-cells  
421 characterised by cytotoxic effectors (*GZMB*, *GZMK*, *IFNG*) and inhibitory markers  
422 (*HAVCR2*, *PDCD1*, *CTLA4*, *LAG3*, *TIGIT*; **Fig. 6c**). C2\_CD8\_GZMKs represented pre-  
423 effector cells as expression of *GZMK* was high, but expression of cytotoxic effectors low.  
424 C3\_CD8\_ZNF683s constituted memory CD8<sup>+</sup> T-cells based on *ZNF683* expression<sup>53</sup>,  
425 while C4\_CD8\_CX3CR1s corresponded to effector T-cells due to high cytotoxic marker  
426 expression. Remarkably, C4s also expressed markers typically observed in NK-cells  
427 (*KLRD1*, *FGFBP2*, *CX3CR1*), suggesting they are endowed with NK T-cell (NKT) activity.  
428 Similarly, based on marker gene expression, we assigned C5\_CD4\_CCR7s to naïve  
429 (*CCR7*, *SELL*, *LEF1*), C6\_CD4\_GZMAs to CD4<sup>+</sup> memory/effector (*GZMA*, *ANXA1*) and  
430 C7\_CD4\_CXCL13s to exhausted CD4<sup>+</sup> effector T-cells (*CXCL13*, *PDCD1*, *CTLA4*, *BTLA*).  
431 Based on *FOXP3* expression C8\_FOXP3s were assigned CD4<sup>+</sup> regulatory T-cells (Tregs).  
432 Finally, two clusters contained NK-cells based on NK- (*NCR1*, *NCAM1*) but not T-cell  
433 (*CD3D*, *CD4*, *CD8A*; **Fig. 6b,c**) marker gene expression. Particularly, C9\_NK\_FGFBP2s  
434 represented cytotoxic NK-cells due to expression of *FGFBP2*, *FCGR3A* and cytotoxic  
435 genes including *GZMB*, *NKG7* and *PRF1*, while C10\_NK\_XCL1s appeared to be less  
436 cytotoxic, but positive for *XCL1* and *XCL2*, two chemo-attractants involved in DC  
437 recruitment enhancing immunosurveillance<sup>54</sup>.

438 Interestingly, T-cell clusters were highly similar to the T-cell taxonomy derived from breast,  
439 liver and lung cancer, despite underlying differences in sample preparation and single-cell  
440 technology (Supplementary information, **Fig. S6e**)<sup>53,55,56</sup>. Indeed, C8 cells could be re-  
441 clustered into CLTA4<sup>high</sup> and CLTA4<sup>low</sup> clusters with corresponding marker genes  
442 (Supplementary information, **Fig. S6f-g**), as reported<sup>53,56</sup>, while also both NK clusters  
443 corresponded to recently identified NK subclusters shared across organs and species<sup>57</sup>.

444 Several T-cell phenotypes, especially those with inhibitory markers, were enriched in  
445 tumour tissue (**Fig. 6d,e**, Supplementary information, **Fig. S6h**). C9\_NK\_FGFBP2s were  
446 more prevalent in normal tissue, suggesting these to represent tissue-patrolling  
447 phenotypes of NK-cells. All T-cell clusters were more frequent in LC, while cytotoxic T-

448 cells were rare in CRC and regulatory T-cells underrepresented in OvC (**Fig. 6f**).  
449 Expression of inhibitory markers (*HAVCR2*, *LAG3*, *PDCD1*) was enhanced in  
450 exhausted/cytotoxic C1\_CD8\_HAVCR2s residing in tumour *versus* normal tissue  
451 (Supplementary information, **Fig. S6i**). We also observed expression of *KLRC1* (*NKG2A*),  
452 a novel checkpoint<sup>58,59</sup> exclusively in C10 NK-cells (**Fig. 6c**). CD8<sup>+</sup> T-cell trajectory analysis  
453 revealed that C2 pre-effector T-cells also contained naïve CD8<sup>+</sup> T-cells, which expressed  
454 *CCR7*, *TFC7* and *SELL*, and formed the root of the trajectory (Supplementary information,  
455 **Fig. S6j,k**). Pre-effector T-cells then differentiated into either exhausted  
456 (C1\_CD8\_HAVCR2) or effector (C4\_CD8\_CX3CR1) T-cells (**Fig. 6g**). Dynamic expression  
457 of marker genes along both trajectories confirmed high expression of *IFNG*, inhibitory and  
458 cytotoxicity markers in the HAVCR2 trajectory (Supplementary information, **Fig. S6l**).  
459 Interestingly, LC CD8<sup>+</sup> T-cells were more differentiated in this trajectory and thus more  
460 exhausted compared to T-cells from CRC and OvC (**Fig. 6h**).

461 TFs underlying each T-/NK-cell phenotype were identified by SCENIC (**Fig. 6i**): for  
462 instance, *FOXP3* was specific for C8s, as expected, while *IRF9*, which induces *PDCD1*<sup>60</sup>,  
463 was increased in exhausted CD8<sup>+</sup> T-cells (C1). C1\_CD8\_HAVCR2 T-cells exhibited high  
464 interferon activation based on cancer hallmark analysis (Supplementary information, **Fig.**  
465 **S6m**), while metabolic pathway analysis revealed upregulation of glycolysis and  
466 nucleotide metabolism in T-cell phenotypes enriched in tumours (C1, C7-C8;  
467 Supplementary information, **Fig. S6n**). Finally, we noticed a negative correlation between  
468 the prevalence of cancer and immune cells, including several T-cell phenotypes  
469 (Supplementary information, **Fig. S3m**). When scoring cancer cells for cancer hallmark  
470 pathways and comparing these scores with stromal cell phenotype abundance, some  
471 remarkable associations were noticed. Specifically, C1\_CD8\_HAVCR2 T-cells were  
472 positively correlated with augmented interferon signalling, inflammation and  
473 IL6/JAK/STAT3 signalling in cancer cells (Supplementary information, **Fig. S6o**).

#### 474 ***Trajectory of monocyte-to-macrophage differentiation revealed***

475 In the 32,721 myeloid cells, we identified 12 unaligned clusters, including 2 monocyte (C1-  
476 C2), 7 macrophage (C3-C9) and 1 neutrophil (C10) clusters (**Fig. 7a,b**). A low-quality  
477 cluster (C11) and myeloid/T-cell doublet cluster (C12\_CD3D) are not discussed  
478 (Supplementary information, **S7a,b**). Only C8 macrophages were tissue-specific, while



479 remaining cells clustered similarly with CCA as with unaligned clustering, expressing the  
480 same marker genes and functional gene sets (**Fig. 7c**, Supplementary information, **Fig.**  
481 **S7c,d**).

482 Monocytes clustered separately from macrophages based on reduced macrophage  
483 marker expression (*CD68*, *MSR1*, *MRC1*) and a phylogenetic reconstruction  
484 (Supplementary information, **Fig. S7e,f**). C1\_CD14 monocytes represented classical  
485 monocytes based on high *CD14* and *S100A8/9* expression and typically are recruited  
486 during inflammation. They expressed the monocyte trafficking factors *SELL* (*CD62L*)  
487 –involved in EC adhesion– and *CCR2*, a receptor for the pro-migratory cytokine *CCL2*.  
488 C2\_CD16s were less abundant and represented non-classical monocytes based on low  
489 *CD14*, but high expression of *FCGR3A* (*CD16*) and other marker genes (*CDKN1C*, *MTSS1*;  
490 Supplementary information, **Fig. S7f**)<sup>61</sup>. C2s constantly patrol the vasculature, express  
491 *CX3CR1* (Supplementary information, **Fig. S7d,g**) and migrate into tissues in response to  
492 *CX3CL1* derived from inflamed ECs.

493 Macrophages are classified based on origin (tissue-resident *versus* recruited) or their pro-  
494 *versus* anti-inflammatory role (M1-like *versus* M2-like, **Fig. 7c**). C3\_CCR2s and C4\_CCL2s  
495 represented early-stage macrophages that were closely-related, not enriched in tumours  
496 (**Fig. 7d** and Supplementary information, **Fig. S7e**) and become replenished by classical  
497 monocytes. Specifically, C3 macrophages represented immature macrophages closely  
498 related to C1 monocytes, as they also express *CCR2* (**Fig. 7b**). They were characterised  
499 by pronounced M1 marker gene expression (*IL1B*, *CXCL9*, *CXCL10*, *SOCS3*; **Fig. 7c**).  
500 C4\_CCL2s were characterised by *CCL2* expression, which is another M1 marker  
501 promoting immune cell recruitment to inflammatory sites. Compared to C3s, C4  
502 macrophages expressed less *CCR2*, but moderate levels of the M2 marker gene *MRC1*,  
503 suggesting an intermediate pro-inflammatory phenotype.

504 Macrophages belonging to C5-C7 clusters were enriched in malignant tissue and  
505 represented tumour-associated macrophages (TAMs, **Fig. 7d**, Supplementary information,  
506 **Fig. S7h**). C5\_CCL18s represented ~72% of all TAMs and were characterised by M2  
507 marker expression, including *CCL18* and *GPNMB* (**Fig. 7c**). Additional heterogeneity  
508 separated C5 cells into intermediate and more differentiated M2 macrophages, although  
509 differences were graded, consistent with a continuous phenotypic spectrum

510 (Supplementary information, **Fig. S7i**). Indeed, there was more pronounced M2 marker  
511 expression (e.g. *SEPP1*, *STAB1*, *CCL13*) in 34% of C5s<sup>62</sup>. These also expressed key  
512 metabolic pathway regulators, i.e. *SLC40A1* (iron), *FOLR2* (folate), *FUCA1* (fucose) and  
513 *PDK4* (pyruvate), linking M2 differentiation with metabolic reprogramming. C6\_MMP9  
514 macrophages expressed a unique subset of M2 markers (*CCL22*, *IL1RN*, *CHI3L1*) and  
515 several MMPs, suggesting a role in tumour tissue remodelling. Cancer hallmark analysis  
516 revealed enrichment in EMT, hypoxia, glycolysis and many other pathways  
517 (Supplementary information, **Fig. S7j**). C7\_CX3CR1 macrophages expressed genes  
518 involved both in M1 and M2 polarization (*CCL3*, *CCL4*, *TNF*, *AXL*, respectively, **Fig. 7c**).  
519 Interestingly, *AXL* is involved in apoptotic cell clearance<sup>63</sup>, whereas other M2 markers  
520 involved in pathogen clearance, i.e. *MRC1* and *CD163*, were absent, suggesting a unique  
521 phagocytic pattern of C7 cells. They are also correlated with poor prognosis in OvC and  
522 CRC<sup>64,65</sup>. Of note, C7 macrophages shared their CD16<sup>high</sup>/CX3CR1<sup>high</sup> phenotype with C2  
523 non-classical monocytes, suggesting both clusters may be related (Supplementary  
524 information, **Fig. S7g**). C8\_PPARG macrophages corresponded to resident alveolar  
525 macrophages due to expression of the resident alveolar macrophage marker *PPARG*.  
526 They were exclusive to normal lung tissue (**Fig. 7d**), expressed established M2 markers  
527 (*MSR1*, *CCL18*, *AXL*)<sup>62,66</sup> in addition to anti-inflammatory genes (*FABP4*, *ALDH2*)<sup>67,68</sup>.  
528 C9\_LYVE1 macrophages also represented resident macrophages with pronounced M2  
529 marker expression and enrichment in normal tissue. They often locate at the  
530 perivascularity of different tissues where they contribute to both angiogenesis and  
531 vasculature integrity<sup>69-71</sup>. Indeed, C9 macrophages expressed the angiogenic factor  
532 *EGFL7*, but also immunomodulators *CD209*, *CH25H* and *LILRB5*, which are implicated in  
533 both innate and adaptive immunity<sup>62,72,73</sup>.

534 Finally, the C10\_FCGR3B cluster represented neutrophils expressing the neutrophil-  
535 specific antigen CD16B (encoded by *FCGR3B*), but not *MPO*, which is typically expressed  
536 in neutrophils during inflammation and microbial infection. C10 cells expressed pro-  
537 inflammatory factors (*CXCL8*, *IL1B*, *CCL3*, *CCL4*; Supplementary information, **Fig. S7g**)  
538 and, in line with their pro-tumour activity, also pro-angiogenic factors (*VEGFA*, *PROK2*)<sup>74</sup>.  
539 Notably, neutrophils were strongly enriched in malignant tissue, but were characterised  
540 by low transcriptional activity (689 detected genes/cell; **Fig. 7d**, Supplementary  
541 information, **Fig. S7b**).

542 Interestingly, except for resident alveolar macrophages (C8), all myeloid clusters were  
543 present in each cancer type, albeit with some preferences (**Fig. 7d,e**). Notably, similar to  
544 other scRNA-seq studies<sup>4,6,7,75</sup>, we also failed to identify myeloid-derived suppressor cells  
545 (MDSCs). To delineate monocyte-to-macrophage differentiation, we performed a  
546 trajectory inference analysis. We excluded non-classical monocytes and related  
547 macrophages (C2, C7), and resident macrophages (C8, C9). In the trajectory, C1  
548 monocytes were progenitor cells for C3 immature macrophages (**Fig. 7f**). Next on the time  
549 scale were C4 macrophages, which further separated into C5 and C6 macrophages,  
550 suggesting C4 macrophages to be endowed with high plasticity prior to M2 differentiation.  
551 Interestingly, LC macrophages were more differentiated in both lineages (Supplementary  
552 information, **Fig. S7k**). Profiling of gene expression dynamics along the trajectory (**Fig.**  
553 **7g,h**) revealed a reduction of known monocyte markers (*CD14*, *S100A8*, *SELL*) and  
554 increased expression of 230 other genes (Supplementary information, **Table S9**),  
555 including several M2 markers. SCENIC identified several TFs underlying each myeloid  
556 phenotype or the monocyte-to-macrophage differentiation trajectory (**Fig. 7i,j** and  
557 Supplementary information, **S7l,m**). For example, there was a gradual increase of *MAFB*  
558 and decrease of *FOS*, *FOSB* and *EGR1* along the trajectory, as reported<sup>76,77</sup>. Interestingly,  
559 terminally differentiated clusters (C5, C6) were characterised by distinct TFs, but also  
560 shared TFs, including the hypoxia-induced HIF-2 $\alpha$  (*EPAS1*; Supplementary information,  
561 **Fig. S7n**)<sup>78</sup>.

562 Finally, we also identified 1,962 mast cells. These cells represent a rare stromal cell type  
563 that was not enriched for in tumours, and that could be subclustered into 4 cellular  
564 phenotypes (Supplementary information, **Fig. S8a-h**).

### 565 ***Mapping the blueprint in breast cancer***

566 In 3 different cancers, we identified 68 stromal cell (sub)types, of which 46 were shared.  
567 To confirm this heterogeneity in another cancer type, we profiled 14 treatment-naïve  
568 breast cancers (BC) using 5'-scRNA-seq and clustered the 44,024 cells with high quality  
569 data (Methods). After assigning cell types (**Fig. 8a**, Supplementary information, **Fig. S9a**),  
570 we re-clustered cells per cell type using unaligned clustering, or after pooling cell type  
571 data from BC with those from other cancer types, while applying CCA alignment for 5'  
572 *versus* 3'-scRNA-seq. Both approaches clustered the 14,413 T-cells from BC into their 10

573 cellular phenotypes, each with similar expression signatures as described for 3'-scRNA-  
574 seq (**Fig. 8b** and Supplementary information, **Fig. S9b**). However, in other cell types  
575 unaligned clustering failed to identify the cellular phenotypes, especially when they were  
576 less abundant. In contrast, CCA recovered 43 out of the 46 shared phenotypes (**Fig. 8b,c**,  
577 Supplementary information, **Fig. S9c**). Only for mast cells, for which too few cells were  
578 detected (n=360), CCA also failed to identify the respective phenotypes. Notably, across  
579 cancer types all cellular phenotypes were characterised by a highly similar expression of  
580 marker genes and underlying TFs (**Fig. 8d,e** and Supplementary information, **Fig. S9d-h**).  
581 These data confirm that the stromal cell blueprint can also be assigned to other cancer  
582 types.

583 When subsequently comparing stromal cell type distribution between BC and all other  
584 cancers, we found more T-cells in BC than CRC or OvC, but not LC (Supplementary  
585 information, **Fig. S9i**). At the subcluster level, BC was enriched for pDCs (C4\_LILRA4), but  
586 had few lymphatic ECs (C5\_PROX1; Supplementary information, **Fig. S9j**). Possibly, this  
587 is because most patients (8/14) had a triple-negative BC, which is more immunogenic,  
588 without lymph node involvement.

### 589 ***The blueprint as a guide to interpret scRNA-seq studies***

590 We also applied our blueprint to SMART-seq2 data from melanomas treated with immune  
591 checkpoint inhibitors (ICIs). We clustered our T-/NK-cells from the blueprint with the  
592 12,681 T-/NK-cells profiled by SMART-seq2<sup>8</sup>, while performing CCA for technology. This  
593 resulted in the 10 T-/NK-cell phenotypes of the blueprint (Supplementary information, **Fig.**  
594 **S10a-c**). Cells profiled by both technologies contributed to every phenotypic T-/NK-cell  
595 cluster, each with similar expression signatures, suggesting effective CCA alignment. Next,  
596 we confirmed findings by Sade-Feldman et al.<sup>8</sup>, showing that *i*) presence of exhausted  
597 CD8<sup>+</sup> T-cells (C1) in melanoma tumours predicts resistance to ICI, while *ii*) increased  
598 expression of the naïve T-cell marker *TCF7* across CD8<sup>+</sup> T-cells predicts response to ICI  
599 (Supplementary information, **Fig. S10d**). However, when assessing *TCF7* in the context of  
600 the blueprint, we found it was expressed in 2 out of 4 CD8<sup>+</sup> T-cell phenotypes (C2-C3), of  
601 which only pre-effector CD8<sup>+</sup> T-cells (C2) were significantly more prevalent in responders  
602 (**Fig. 8f,g**). Additionally, *TCF7* expression was high in naïve CD4<sup>+</sup> T-cells (C5), which were  
603 also enriched in responders ( $p=0.0021$ ). Receiver operating characteristic (ROC) analysis

604 to evaluate the predictive effect of the C5 cluster revealed an AUC of 0.90 ( $p=0.0021$ ; **Fig.**  
605 **8h**). Albeit to a lesser extent, C1 and C2 clusters were also enriched in non-responders  
606 and responders, respectively (Supplementary information, **Fig. S10e**). Notably, CD4<sup>+</sup>  
607 TCF7<sup>+</sup> T-cells resided outside of blood vessels, within the tumour at the peritumoral front  
608 (Supplementary information, **Fig. S10f**).

609 Next, we applied our blueprint to monitor changes in T-/NK-cells during ICI. When  
610 comparing pre- *versus* on-treatment biopsies (n=4 with response *versus* n=6 without  
611 response), we observed an increase in exhausted CD8<sup>+</sup> T-cells (C1\_CD8\_HAVCR2) in on-  
612 treatment biopsies. *Vice versa*, there was a relative decrease in naïve CD4<sup>+</sup>  
613 (C5\_CD4\_CCR7) T-cells (Supplementary information, **Fig. S10g,h**). Notably, these  
614 differences were only observed in responding patients, suggesting that during response,  
615 phenotypic clusters that predict resistance in the pre-treatment biopsy increase, while  
616 those predicting response decrease in prevalence. Overall, these data illustrate that  
617 single-cell data obtained with various technologies can be re-analysed in the context of  
618 the blueprint.

### 619 ***Validation of the blueprint at protein level***

620 With the availability of CITE-seq, we can now simultaneously detect RNA and protein  
621 expression at single-cell level<sup>79</sup>. To confirm the cancer blueprint at protein level, a panel  
622 of 198 antibodies (Supplementary information, **Table S10**) compatible with 3'-scRNA-seq  
623 was used. We processed 5 BCs, obtaining 6,194 cells with both transcriptome and  
624 proteome data. Independent clustering of both datasets revealed how cell types could be  
625 discerned based on either marker gene or protein expression (**Fig. 9a,b**). Since antibodies  
626 were mainly directed against immune cells, especially T-cells, we focused our  
627 subclustering efforts on this cell type. We pooled 1,310 T-/NK-cells with both RNA and  
628 protein data together with T-/NK-cells from the blueprint. Subsequent clustering based  
629 on scRNA-seq data accurately assigned each T-/NK-cell to its phenotypic cluster  
630 (**Fig.9c,d**). Next, we selected marker genes amongst the 198 antibodies and explored  
631 protein expression per cluster (**Fig. 9e**). A combination of CD3, CD4, CD8 and NCR1  
632 effectively discriminated CD4<sup>+</sup>, CD8<sup>+</sup> T-cells and NK-cells. The T-cell exhaustion marker  
633 PD-1 discriminated exhausted CD4<sup>+</sup> and CD8<sup>+</sup> T-cell phenotypes (C1, C7), while IL2RA  
634 (CD25) was specific for CD4<sup>+</sup> Tregs (C8). CD8<sup>+</sup> memory T-cells (C3) were characterised

635 by high ITGA1 but low PDCD1. Both the cytotoxic T-/NK-cells (C4, C9) had high levels of  
636 KLRG1, while CD4<sup>+</sup> naïve cells had high ITGA6 and SELL (C5). Unfortunately, there were  
637 no antibodies specific for C2 and C6 cells. Despite this limitation, a random forest model  
638 developed to predict major cell types and T-cell phenotypes based on CITE-seq  
639 classified >80% of cells into the same cell (sub)type compared to scRNA-seq data.

640

## 641 **DISCUSSION**

642 Here, we performed scRNA-seq on 233,591 single cells from 36 patients with either lung,  
643 colon, ovarian or breast cancer. By applying two different clustering approaches –one  
644 designed to detect tissue-specific differences, the other to find shared heterogeneity  
645 amongst stromal cell types– we constructed a pan-cancer blueprint of stromal cell  
646 heterogeneity. Briefly, we found that tissue-resident cell types, including ECs and  
647 fibroblasts, were characterised by considerable patient and tissue specificity in the normal  
648 tissue, but that part of this heterogeneity disappeared within the TME. On the other hand,  
649 phenotypes involving non-residential cell types, which encompass most of the tumour-  
650 infiltrating immune cells, were often shared amongst all patients and cancer types. Overall,  
651 we identified 68 stromal phenotypes, of which 46 were shared between cancer types and  
652 22 were cancer type-unique. Amongst the shared phenotypes, several have not previously  
653 been described at single-cell level, including tumour-associated pericytes and other  
654 fibroblast phenotypes, mast cells, GC-independent B-cells, neutrophils, *etc.* Of note, by  
655 applying a CITE-seq approach to simultaneously profile gene and protein expression, we  
656 confirmed all major cell types and T-cell phenotypes identified by scRNA-seq.

657 An important merit of our study is the public availability of the scRNA-seq data and the  
658 stromal blueprint we describe, which can all be interactively accessed via our blueprint  
659 server. This will allow scientists to co-cluster their own scRNA-seq data together with  
660 blueprint data and assign each of their individual cells to a cellular phenotype. This can  
661 also be achieved by feeding our stromal blueprint dataset to established machine learning  
662 pipelines, e.g. CellAssign<sup>80</sup>, and assigning each new cell to the most likely proxy. Such  
663 strategy would indeed be highly relevant, as several of our cellular phenotypes are missed  
664 when a smaller number of cells is analysed. Interestingly, as illustrated for melanoma,  
665 pooling new with existing scRNA-seq data was even possible when a different single-cell

666 technology was used. Similarly, this blueprint could serve as training matrix to estimate  
667 the prevalence from specific cell (sub)types in bulk tissue transcriptomes using newly  
668 developed deconvolution methods, i.e. CIBERSORTx<sup>81</sup>. This is important, as bulk RNA-  
669 seq data of tumour tissues are often available for multiple large and homogeneous cohorts  
670 of cancer patients.

671 We also built trajectories between relevant cell phenotypes, highlighting how several of  
672 these do not represent separate entities. Stratification of these trajectories for cancer type  
673 revealed some intriguing differences. For instance, LC contained more exhausted CD8<sup>+</sup>  
674 cytotoxic T-cells in the C1\_CD8\_HAVCR2 trajectory. Moreover, LC appeared more  
675 inflammatory as it was enriched for differentiated myeloid cells along both the CCL18 and  
676 MMP9 lineage. Also, memory B-cells were more differentiated in LC, while cDC2s got  
677 stuck early in the trajectory in OvC. Most probably, these differences are due to the fact  
678 that LC is an immune-infiltrated cancer with a high tumour mutation burden (TMB) and  
679 neoepitope load<sup>82</sup>, while OvC and CRC are cold tumours with a low TMB.

680 We believe our blueprint is also useful when monitoring dynamic changes in the TME  
681 during cancer treatment. Indeed, by performing scRNA-seq on individual biopsies  
682 obtained before and during treatment, individual cells can be assigned to each phenotypic  
683 cluster and changes can easily be interpreted in the context of the blueprint. For instance,  
684 when re-analysing a set of pre- *versus* on-treatment biopsies from melanomas exposed  
685 ICIs, we observed that exhausted CD8<sup>+</sup> T-cells became gradually more common during  
686 treatment, while naïve CD4<sup>+</sup> T-cells became less common. Notably, these shifts were only  
687 observed in patients responding to the treatment. Although findings that naïve CD4<sup>+</sup>  
688 helper T-cells predict checkpoint immunotherapy are novel, these findings are not  
689 unexpected. Firstly, CD4<sup>+</sup> helper T-cells can also express PD1, and are thus targeted by  
690 the treatment. Furthermore, they can enhance CD8<sup>+</sup> T-cell infiltration<sup>83</sup>, improve antibody  
691 penetration<sup>84</sup>, T-cell memory formation, or have a direct cytolytic capacity<sup>85</sup>. Several other  
692 studies suggest the role of both naïve CD4<sup>+</sup> and CD8<sup>+</sup> T-cells in priming anti-tumour  
693 activity<sup>86</sup>. Overall, we believe that our approach to monitor how blueprint phenotypes  
694 change in response to cancer treatment and gradually also contribute to therapeutic  
695 resistance, will allow scientists to gain important insights into the mechanisms of action  
696 of novel cancer drugs.

## 697 **MATERIALS AND METHODS**

### 698 **Patients**

699 This study was approved by the local ethics committee at the University Hospital Leuven  
700 for each cancer type. Only patients provided with informed consent were included in this  
701 study. The clinical information of all patients was summarised in **Table S1**.

### 702 **Preparation of single-cell suspensions**

703 Following resection, samples from the tumour and adjacent non-malignant tissue were  
704 rapidly processed for single-cell RNA-sequencing. Samples were rinsed with PBS,  
705 minced on ice to pieces of  $<1\text{ mm}^3$  and transferred to 10ml digestion medium containing  
706 collagenase P ( $2\text{ mg ml}^{-1}$ , ThermoFisher Scientific) and DNase I ( $10\text{ U } \mu\text{l}^{-1}$  Sigma) in DMEM  
707 (ThermoFisher Scientific). Samples were incubated for 15min at  $37^\circ\text{C}$ , with manual  
708 shaking every 5min. Samples were then vortexed for 10s and pipetted up and down for  
709 1min using pipettes of descending sizes (25ml, 10ml and 5ml). Next, 30ml ice-cold PBS  
710 containing 2% fetal bovine serum was added and samples were filtered using a  $40\mu\text{m}$   
711 nylon mesh (ThermoFisher Scientific). Following centrifugation at  $120\times g$  and  $4^\circ\text{C}$  for 5min,  
712 the supernatant was decanted and discarded, and the cell pellet was resuspended in red  
713 blood cell lysis buffer. Following a 5-min incubation at room temperature, samples were  
714 centrifuged ( $120\times g$ ,  $4^\circ\text{C}$ , 5min) and resuspended in 1ml PBS containing  $8\mu\text{l}$  UltraPure  
715 BSA ( $50\text{ mg ml}^{-1}$ ; AM2616, ThermoFisher Scientific) and filtered over Flowmi  $40\mu\text{m}$  cell  
716 strainers (VWR) using wide-bore 1ml low-retention filter tips (Mettler-Toledo). Next,  $10\mu\text{l}$   
717 of this cell suspension was counted using an automated cell counter (Luna) to determine  
718 the concentration of live cells. The entire procedure was completed in less than 1h  
719 (typically about 45 min).

### 720 **Single cell RNA-seq data acquisition and pre-processing**

721 Libraries for scRNA-seq were generated using the Chromium Single Cell 3' or 5' library  
722 and Gel Bead & Multiplex Kit from 10x Genomics (**Table S2**). We aimed to profile 5,000  
723 cells per library (if sufficient cells were retained during dissociation). All libraries were  
724 sequenced on Illumina NextSeq, HiSeq4000 or NovaSeq6000 until sufficient saturation  
725 was reached (73.8% on average, **Table S2**). After quality control, raw sequencing reads  
726 were aligned to the human reference genome GRCh38 and processed to a matrix  
727 representing the UMI's per cell barcode per gene using CellRanger (10x Genomics, v2.0).



## 728 **Single-cell RNA analysis to determine major cell types and cell phenotypes**

729 Raw gene expression matrices generated per sample were merged and analysed with the  
730 Seurat package (v2.3.4). Matrices were filtered by removing cell barcodes with <401 UMIs,  
731 <201 expressed genes, >6,000 expressed genes or >25% of reads mapping to  
732 mitochondrial RNA. The remaining cells were normalized and genes with a normalized  
733 expression between 0.125 and 3, and a quantile-normalized variance >0.5 were selected  
734 as variable genes. The number of variably-expressed genes differs for each clustering  
735 step (**Table S4**). When clustering cell types, we regressed out confounding factors:  
736 number of UMIs, % of mitochondrial RNA, patient ID and cell cycle (S and G2M phase  
737 scores calculated by the CellCycleScoring function in Seurat). After regression for  
738 confounding factors, all variably-expressed genes were used to construct principal  
739 components (PCs) and PCs covering the highest variance in the dataset were selected.  
740 The selection of these PCs was based on elbow and Jackstraw plots. Clusters were  
741 calculated by the FindClusters function with a resolution between 0.2 and 2, and  
742 visualised using the t-SNE dimensional reduction method. Differential gene-expression  
743 analysis was performed for clusters generated at various resolutions by both the Wilcoxon  
744 rank sum test and Model-based Analysis of Single-cell Transcriptomics (MAST) using the  
745 FindMarkers function. A specific resolution was selected when known cell types were  
746 identified as a cluster at a given resolution, but not at a lower resolution (**Table S5**), with  
747 the minimal constraint that each cluster has at least 10 significantly differentially  
748 expressed genes (FDR<0.01 with both methods) with at least a 2-fold difference in  
749 expression compared to all other clusters. Annotation of the resulting clusters to cell types  
750 was based on the expression of marker genes (Supplementary information, **Fig. S1c**). All  
751 major cell types were identified in one clustering step, except for DCs; pDCs co-clustered  
752 with B-cells, while other DCs co-clustered with myeloid cells. Therefore, we first separated  
753 DCs per cancer type based on established marker genes (pDC: *LILRA4* and *CXCR3*; cCDs:  
754 *CLEC9A*, *XCR1*, *CD1C*, *CCR7*, *CCL17*, *CCL19*, Langerhans-like: *CD1A*, *CD207*)<sup>2,40</sup> and  
755 then pooled these DCs for subclustering.

756 Next, all cells assigned to a given cell type per cancer type were merged and further  
757 subclustered into functional phenotypes using the same strategy, which we refer to as the  
758 unaligned clustering approach in the manuscript. However, the confounding factors used  
759 for cell types were not sufficient to reduce patient-specific effects when performing the

760 subclustering. Instead of directly applying an unsupervised batch correction algorithm,  
761 we found that the interferon response (BROWNE\_INTERFERON\_RESPONSIVE\_GENES  
762 in the Molecular Signatures Database or MSigDB v6.2) and the sample dissociation-  
763 induced gene signatures<sup>87</sup> represent common patient-specific confounders, which were  
764 therefore regressed out. We additionally regressed out the hypoxia signature<sup>88</sup> for myeloid  
765 cells to avoid clusters driven by hypoxia state instead of its origin or (anti-)inflammatory  
766 functions. Since hemoglobin and immunoglobulin genes are common contaminants from  
767 ambient RNA, hemoglobin genes were excluded for PCA. This also applied to  
768 immunoglobulin genes, except when subclustering B-cells. For T-cell subclustering,  
769 variable genes of T-cell receptor (*TRAVs*, *TRBVs*, *TRDVs*, *TRGVs*) were excluded to avoid  
770 somatic hypermutation associated variances. Similarly, variable genes of B-cell receptor  
771 (*IGLVs*, *IGKVs*, *IGHVs*) were all excluded when subclustering B-cells.

772 To reveal similarities between the subclusters across cancer types, we performed  
773 canonical correlation analysis (CCA, RunMultiCCA function) by aligning data from different  
774 cancer types into a subspace with the maximal correlation<sup>11</sup>. The selection of CCA  
775 dimensions or canonical correction vectors (CCs) for subspace alignment were guided by  
776 the CC bicor saturation plot (MetageneBicorPlot function). Resolution was determined  
777 similar to the PCA-based approach described above, followed by marker gene-based  
778 cluster annotation. Since CCA is designed to identify shared clusters, we performed CCA  
779 alignment without cancer-type specific cells defined by PCA-based approach for  
780 fibroblasts and myeloid cells. Low quality clusters were identified based on the number of  
781 detected genes within subclusters and the lack of marker genes. Doublet clusters  
782 expressed marker genes from other cell lineages, and had a higher than expected (3.9%  
783 according to the User Guide from 10x Genomics) doublets rate, as predicted by the  
784 artificial k-nearest neighbours algorithm implemented in DoubletFinder (v1.0)<sup>89</sup>. We also  
785 used Scrublet<sup>90</sup> to identify doublet cells and could predict the same clusters as predicted  
786 by DoubletFinder. As an example, we evaluate for each of the B-cell clusters, *i*) the  
787 expression of marker genes from other cell types, *ii*) the higher number of detected genes,  
788 and *iii*) the overlap of cells predicted to be doublets by DoubletFinder and Scrublet  
789 (Supplementary Information, **Fig. S11a-d**).

790 For a comprehensive statistical analysis, we used a single-cell specific method based on  
791 mixed-effects modelling of associations of single cells (MASC) (Fonseka et al., 2018). The

792 analysis systematically addressed two major questions: which cell types are enriched or  
793 depleted in all cancers or in a particular cancer type, and which cell types or stromal  
794 phenotypes are enriched or depleted in tumours versus normal tissue in all cancers or in  
795 a particular cancer type. Events with  $FDR < 0.05$  were considered significant as  
796 summarised in **Table S6**.

#### 797 **SCENIC analysis**

798 Transcription factor (TF) activity was analysed using SCENIC (v1.0.0.3) per cell type with  
799 raw count matrices as input. The regulons and TF activity (AUC) for each cell were  
800 calculated with the pySCENIC (v0.8.9) pipeline with motif collection version mc9nr. The  
801 differentially activated TFs of each subcluster were identified by the Wilcoxon rank sum  
802 test against all the other cells of the same cell type. TFs with log-fold-change  $>0.1$  and an  
803 adjusted p-value  $<1e-5$  were considered as significantly upregulated.

#### 804 **Trajectory inference analysis**

805 We applied the Monocle (v2.8.0) algorithm to determine the potential lineage between  
806 diverse stromal cell phenotypes<sup>91</sup>. Seurat objects were imported to Monocle using  
807 importCDS function. DDRTree-based dimension reduction was performed with conserved  
808 and differentially expressed genes. These genes were calculated for each subcluster  
809 across LC, CRC and OvC using FindConservedMarkers function in Seurat using the  
810 metap (v1.0) algorithm and Wilcoxon rank sum test ( $max\_pval < 0.01$ ,  $minimum\_p\_val <$   
811  $1e-5$ ). PC selection was determined using the PC variance plot  
812 (`plot_pc_variance_explained` function in Monocle, 3-5 PCs). Genes with branch-  
813 dependent expression dynamics were calculated using the BEAM test in Monocle. Genes  
814 with a q-value  $<1e-10$  were plotted in heatmaps. The dynamics of transcription factor  
815 activity (or AUC) was calculated by SCENIC and plotted per branch of trajectory along the  
816 pseudotime calculated by Monocle. For each TF, the AUC and pseudotime, smoothed as  
817 a natural spline using `sm.ns` function, were fitted in vector generalised linear model (VGLM)  
818 using VGAM package v1.1. TF with q-value  $<1e-50$  were selected for plotting. Two other  
819 trajectory inference pipelines, i.e., Slingshot and SCORPIUS<sup>92,93</sup>, were also used. Since  
820 SCORPIUS cannot handle branched trajectories, we analysed both trajectories separately  
821 with the branching topology informed by Monocle analysis. To assess consistency  
822 between these pipelines, scaled pseudotime between Monocle, Slingshot and SCORPIUS  
823 were compared and high correlations were consistently observed between all lineages.

824 Additionally, we compared expression of key marker genes along the trajectories of all 3  
825 tools (Supplementary Information, **Fig. S12a-k**).

### 826 **Metabolic and cancer hallmark pathways and geneset enrichment analysis**

827 Metabolic pathway activities were estimated with gene signatures from a curated  
828 database<sup>94</sup>. For robustness of the analysis, lowly expressed genes (< 1% cells) or genes  
829 shared by multiple pathways were trimmed. And pathways with less than 3 genes were  
830 excluded. Cancer hallmark gene sets from Molecular Signatures Database (MSigDB v6.1)  
831 were used. The activity of individual cells for each gene set was estimated by AUCell  
832 package (v1.2.4). The differentially activated pathways of each subcluster were identified  
833 by running the Wilcoxon rank sum test against other cells of the same cell type. Pathways  
834 with log-fold-change > 0.05 and an adjusted p-value < 0.01 were considered as  
835 significantly upregulated. GO and REACOTOME geneset enrichment analysis were  
836 performed using hypeR package<sup>95</sup>, geneset over-representation was determined by  
837 hypergeometric test.

### 838 **CITE-seq**

839 We adopted the established CITE-seq protocol<sup>79</sup> with some modifications. Briefly,  
840 100,000–500,000 single cells of breast tumours were suspended in 100µl staining buffer  
841 (2% BSA, 0.01% Tween in PBS) before adding 10µl Fc-blocking reagent (FcX, BioLegend).  
842 and incubating during 10min on ice. This was followed by the addition of 25µl TotalSeq-  
843 A (Biolegend) antibody-oligo pool (1:1000 diluted in staining buffer) and another 30min  
844 incubation on ice. Cells were washed 3 times with staining buffer and filtered through a  
845 40µm flowmi strainer before processing with 3'-scRNA-seq library kits. ADT (Antibody-  
846 Derived Tags) additive primers were added to increase yield of the ADT product. ADT-  
847 derived and mRNA-derived cDNAs were separated by SPRI purification and amplified for  
848 library construction and subsequent sequencing. For each cell barcode detected in the  
849 corresponding RNA library, ADTs were counted in the raw sequencing reads of CITE-seq  
850 experiments using CITE-seq-Count version 1.4. In the resulting UMI per ADT matrix, the  
851 noise level was calculated for each cell by taking the average signal increased with 3x the  
852 standard deviation of 10 control probes. Signals below this level were excluded. We  
853 divided the UMIs by the total UMI count for each cell to account for differences in library  
854 size and a centred log-ratio (CLR) normalization specific for each gene was computed.  
855 Clustering of protein data was done using the Euclidean distance matrix between cells

856 and t-SNE coordinates were calculated using this distance matrix. The random forest  
857 algorithm incorporated in Seurat was iteratively applied on a training and test set,  
858 consisting of 67% and 33% of cells respectively, to predict cell type and T-/NK-cell  
859 phenotypes.

### 860 **Immunofluorescence assay and analysis**

861 A 5µm-section of a formalin-fixed, paraffin-embedded (FFPE) microarray containing 14  
862 melanoma metastasis from 9 patients was stained with antibodies against SOX10 (SCBT;  
863 sc-365692), CD4 (abcam; ab133616), CD31 (LSBio; LS-C173974) and TCF7 (R&D  
864 systems; AF5596) at a concentration of 1 µg/ml according to the Multiple Iterative Labeling  
865 by Antibody Neodeposition (MILAN) protocol, as described<sup>96</sup>.

### 866 **Tumour mutation detection**

867 Whole-exome sequencing was performed as described previously<sup>97</sup>. The average  
868 sequencing depth was 161±67x coverage. Mutation of CRC samples were detected using  
869 Illumina Trusight26 Tumour kit.

### 870 **Data Availability**

871 Raw sequencing reads of the single-cell RNA experiments have been deposited in the  
872 ArrayExpress database at EMBL-EBI and will be made accessible upon publication. An  
873 interactive web server for scRNA-seq data visualisation and exploration, based on SCoPe  
874 package<sup>98</sup>, is available at <http://blueprint.lambrechtslab.org>.

875

### 876 **Acknowledgements**

877 We thank T. Van Brussel, R. Schepers, and E. Vanderheyden for technical assistance. This  
878 work was supported by a VIB TechWatch Grant to D.L. and B.T., ERC Consolidator Grants  
879 to D.L. (CHAMELEON), Funds for Research - Flanders grants to D.L. (G065615N), KU  
880 Leuven grants to D.L. and to B.T. (BOFZAP) and a VIB Grand Challenge grant to D.L. The  
881 computational resources used in this work were provided by the Flemish Supercomputer  
882 Center (VSC), funded by the Hercules Foundation and the Flemish Government,  
883 Department of Economy, Science and Innovation (EWI) and Stichting tegen Kanker (STK).

884

885

886 **Author Contributions**

887 J.Q. and D.L. designed and supervised the study and wrote the manuscript; J.Q. and B.B.  
888 performed data analysis with significant contributions from P.B. and J.X.; I.V., A.S., S.T.  
889 and E.W. coordinated sample collection and clinical annotation with assistance from S.O.,  
890 H.V., E.E., V.P., S.V., A.B., M.V.B., A.F. and G.F.; F.M.B., Y.V.H. and A.A. performed  
891 MILAN for melanoma samples. Dam.L. and B.T. contributed with critical data  
892 interpretation. All the authors have read the manuscript and provided useful comments.

893

894 **Declaration of Interests**

895 The authors declare no competing interests.

896 **Reference:**

- 897 1. Tirosh, I. *et al.* Dissecting the multicellular ecosystem of metastatic melanoma  
898 by single-cell RNA-seq. *Science* **352**, 189–96 (2016).
- 899 2. Lambrechts, D. *et al.* Phenotype molding of stromal cells in the lung tumor  
900 microenvironment. *Nat. Med.* **24**, 1277–1289 (2018).
- 901 3. Puram, S. V. *et al.* Single-Cell Transcriptomic Analysis of Primary and  
902 Metastatic Tumor Ecosystems in Head and Neck Cancer. *Cell* **171**, 1611-  
903 1624.e24 (2017).
- 904 4. Aizarani, N. *et al.* A human liver cell atlas reveals heterogeneity and epithelial  
905 progenitors. *Nature* **572**, 199–204 (2019).
- 906 5. Venteicher, A. S. *et al.* Decoupling genetics, lineages, and microenvironment  
907 in IDH-mutant gliomas by single-cell RNA-seq. *Science* **355**, eaai8478 (2017).
- 908 6. Hovestadt, V. *et al.* Resolving medulloblastoma cellular architecture by single-  
909 cell genomics. *Nature* **572**, 74–79 (2019).
- 910 7. Peng, J. *et al.* Single-cell RNA-seq highlights intra-tumoral heterogeneity and  
911 malignant progression in pancreatic ductal adenocarcinoma. *Cell Res.* **29**,  
912 725–738 (2019).
- 913 8. Sade-Feldman, M. *et al.* Defining T Cell States Associated with Response to  
914 Checkpoint Immunotherapy in Melanoma. *Cell* **175**, 998-1013.e20 (2018).
- 915 9. Parikh, K. *et al.* Colonic epithelial cell diversity in health and inflammatory  
916 bowel disease. *Nature* **567**, 49–55 (2019).
- 917 10. Cohen, M. *et al.* Lung Single-Cell Signaling Interaction Map Reveals Basophil  
918 Role in Macrophage Imprinting. *Cell* **175**, 1031-1044.e18 (2018).
- 919 11. Butler, A., Hoffman, P., Smibert, P., Papalexi, E. & Satija, R. Integrating single-  
920 cell transcriptomic data across different conditions, technologies, and  
921 species. *Nat. Biotechnol.* **36**, 411–420 (2018).
- 922 12. Pusztaszeri, M. P., Seelentag, W. & Bosman, F. T. Immunohistochemical  
923 expression of endothelial markers CD31, CD34, von Willebrand factor, and  
924 Fli-1 in normal human tissues. *J. Histochem. Cytochem.* **54**, 385–395 (2006).
- 925 13. Müller, A. M., Skrzynski, C., Skipka, G. & Müller, K.-M. Expression of von  
926 Willebrand Factor by Human Pulmonary Endothelial Cells in vivo. *Respiration*  
927 **69**, 526–533 (2002).

- 928 14. Dhaun, N. & Webb, D. J. Endothelins in cardiovascular biology and  
929 therapeutics. *Nat. Rev. Cardiol.* 2019 **6**, 1 (2019).
- 930 15. Strickland, L. A. *et al.* Plasmalemmal vesicle-associated protein (PLVAP) is  
931 expressed by tumour endothelium and is upregulated by vascular endothelial  
932 growth factor-A (VEGF). *J. Pathol.* **206**, 466–475 (2005).
- 933 16. Rupp, C. *et al.* IGFBP7, a novel tumor stroma marker, with growth-promoting  
934 effects in colon cancer through a paracrine tumor-stroma interaction.  
935 *Oncogene* **34**, 815–825 (2015).
- 936 17. van Beijnum, J. R. Gene expression of tumor angiogenesis dissected: specific  
937 targeting of colon cancer angiogenic vasculature. *Blood* **108**, 2339–2348  
938 (2006).
- 939 18. Aibar, S. *et al.* SCENIC: Single-cell regulatory network inference and  
940 clustering. *Nat. Methods* **14**, 1083–1086 (2017).
- 941 19. Eelen, G. *et al.* Endothelial Cell Metabolism. *Physiol. Rev.* **98**, 3–58 (2018).
- 942 20. Kalluri, R. The biology and function of fibroblasts in cancer. *Nat. Rev. Cancer*  
943 **16**, 582–598 (2016).
- 944 21. Kurahashi, M. *et al.* A functional role for the ‘fibroblast-like cells’ in  
945 gastrointestinal smooth muscles. *J. Physiol.* **589**, 697–710 (2011).
- 946 22. Lee, H., Koh, B. H., Peri, L. E., Sanders, K. M. & Koh, S. D. Purinergic  
947 inhibitory regulation of murine detrusor muscles mediated by PDGFR $\alpha$  +  
948 interstitial cells. *J. Physiol.* **592**, 1283–1293 (2014).
- 949 23. Puddifoot, C. A., Wu, M., Sung, R.-J. & Joiner, W. J. Ly6h Regulates  
950 Trafficking of Alpha7 Nicotinic Acetylcholine Receptors and Nicotine-Induced  
951 Potentiation of Glutamatergic Signaling. *J. Neurosci.* **35**, 3420–3430 (2015).
- 952 24. Kinchen, J. *et al.* Structural Remodeling of the Human Colonic Mesenchyme  
953 in Inflammatory Bowel Disease. *Cell* **175**, 372–386.e17 (2018).
- 954 25. Fujisawa, M. *et al.* Ovarian stromal cells as a source of cancer-associated  
955 fibroblasts in human epithelial ovarian cancer: A histopathological study.  
956 *PLoS One* **13**, 1–15 (2018).
- 957 26. Jabara, S. *et al.* Stromal cells of the human postmenopausal ovary display a  
958 distinctive biochemical and molecular phenotype. *J. Clin. Endocrinol. Metab.*  
959 **88**, 484–492 (2003).



- 960 27. Pisarska, M. D., Barlow, G. & Kuo, F. T. Minireview: Roles of the forkhead  
961 transcription factor FOXL2 in granulosa cell biology and pathology.  
962 *Endocrinology* **152**, 1199–1208 (2011).
- 963 28. Rynne-Vidal, A. *et al.* Mesothelial-to-mesenchymal transition as a possible  
964 therapeutic target in peritoneal metastasis of ovarian cancer. *J. Pathol.* **242**,  
965 140–151 (2017).
- 966 29. Saunders, W. B. *et al.* Coregulation of vascular tube stabilization by  
967 endothelial cell TIMP-2 and pericyte TIMP-3. *J. Cell Biol.* **175**, 179–191 (2006).
- 968 30. Salzer, M. C. *et al.* Identity Noise and Adipogenic Traits Characterize Dermal  
969 Fibroblast Aging. *Cell* **175**, 1575–1590.e22 (2018).
- 970 31. Haudenschild, D. R. *et al.* Enhanced Activity of Transforming Growth Factor  
971  $\beta$ 1 (TGF- $\beta$ 1) Bound to Cartilage Oligomeric Matrix Protein. *J. Biol. Chem.* **286**,  
972 43250–43258 (2011).
- 973 32. Staudacher, J. J. *et al.* Activin signaling is an essential component of the TGF-  
974  $\beta$  induced pro-metastatic phenotype in colorectal cancer. *Sci. Rep.* **7**, 1–9  
975 (2017).
- 976 33. Simone, T. & Higgins, P. Inhibition of SERPINE1 Function Attenuates Wound  
977 Closure in Response to Tissue Injury: A Role for PAI-1 in Re-Epithelialization  
978 and Granulation Tissue Formation. *J. Dev. Biol.* **3**, 11–24 (2015).
- 979 34. Ghahary, A. *et al.* Mannose-6-phosphate/IGF-II receptors mediate the effects  
980 of IGF-1-induced latent transforming growth factor  $\beta$ 1 on expression of type I  
981 collagen and collagenase in dermal fibroblasts. *Growth Factors* **17**, 167–176  
982 (2000).
- 983 35. Brett, A., Pandey, S. & Fraizer, G. The Wilms' tumor gene (WT1) regulates E-  
984 cadherin expression and migration of prostate cancer cells. *Mol. Cancer* **12**,  
985 1–13 (2013).
- 986 36. Volksdorf, T. *et al.* Tight Junction Proteins Claudin-1 and Occludin Are  
987 Important for Cutaneous Wound Healing. *Am. J. Pathol.* **187**, 1301–1312  
988 (2017).
- 989 37. Chim, S. M. *et al.* EGFL6 Promotes Endothelial Cell Migration and  
990 Angiogenesis through the Activation of Extracellular Signal-regulated Kinase.  
991 *J. Biol. Chem.* **286**, 22035–22046 (2011).

- 992 38. Orimo, A. *et al.* Stromal Fibroblasts Present in Invasive Human Breast  
993 Carcinomas Promote Tumor Growth and Angiogenesis through Elevated  
994 SDF-1/CXCL12 Secretion. *Cell* **121**, 335–348 (2005).
- 995 39. Nabet, B. Y. *et al.* Exosome RNA Unshielding Couples Stromal Activation to  
996 Pattern Recognition Receptor Signaling in Cancer. *Cell* **170**, 352–366.e13  
997 (2017).
- 998 40. Villani, A.-C. *et al.* Single-cell RNA-seq reveals new types of human blood  
999 dendritic cells, monocytes, and progenitors. *Science* **356**, eaah4573 (2017).
- 1000 41. Guilliams, M. *et al.* Unsupervised High-Dimensional Analysis Aligns Dendritic  
1001 Cells across Tissues and Species. *Immunity* **45**, 669–684 (2016).
- 1002 42. Merad, M., Ginhoux, F. & Collin, M. Origin, homeostasis and function of  
1003 Langerhans cells and other langerin-expressing dendritic cells. *Nat. Rev.*  
1004 *Immunol.* **8**, 935–947 (2008).
- 1005 43. Chopin, M. *et al.* Langerhans cells are generated by two distinct PU.1-  
1006 dependent transcriptional networks. *J. Exp. Med.* **210**, 2967–2980 (2013).
- 1007 44. Geissmann, F. *et al.* Retinoids regulate survival and antigen presentation by  
1008 immature dendritic cells. *J. Exp. Med.* **198**, 623–34 (2003).
- 1009 45. Wu, C. H., Huang, T. C. & Lin, B. F. Folate deficiency affects dendritic cell  
1010 function and subsequent T helper cell differentiation. *J. Nutr. Biochem.* **41**,  
1011 65–72 (2017).
- 1012 46. Salaun, B. *et al.* Cloning and characterization of the mouse homologue of the  
1013 human dendritic cell maturation marker CD208/DC-LAMP. *Eur. J. Immunol.*  
1014 **33**, 2619–2629 (2003).
- 1015 47. Gatto, D., Wood, K. & Brink, R. EBI2 operates independently of but in  
1016 cooperation with CXCR5 and CCR7 to direct B cell migration and organization  
1017 in follicles and the germinal center. *J. Immunol.* **187**, 4621–8 (2011).
- 1018 48. Takemori, T., Kaji, T., Takahashi, Y., Shimoda, M. & Rajewsky, K. Generation  
1019 of memory B cells inside and outside germinal centers. *Eur. J. Immunol.* **44**,  
1020 1258–1264 (2014).
- 1021 49. Shi, G.-X., Harrison, K., Wilson, G. L., Moratz, C. & Kehrl, J. H. RGS13  
1022 Regulates Germinal Center B Lymphocytes Responsiveness to CXC  
1023 Chemokine Ligand (CXCL)12 and CXCL13. *J. Immunol.* **169**, 2507–2515

- 1024 (2002).
- 1025 50. Cyster, J. G. & Allen, C. D. C. B Cell Responses: Cell Interaction Dynamics  
1026 and Decisions. *Cell* **177**, 524–540 (2019).
- 1027 51. Turqueti-Neves, A. *et al.* B-cell-intrinsic STAT6 signaling controls germinal  
1028 center formation. *Eur. J. Immunol.* **44**, 2130–2138 (2014).
- 1029 52. Gustafson, C. E. *et al.* Limited expression of APRIL and its receptors prior to  
1030 intestinal IgA plasma cell development during human infancy. *Mucosal*  
1031 *Immunol.* **7**, 467–477 (2014).
- 1032 53. Guo, X. *et al.* Global characterization of T cells in non-small-cell lung cancer  
1033 by single-cell sequencing. *Nat. Med.* **24**, 978–985 (2018).
- 1034 54. Böttcher, J. P. *et al.* NK Cells Stimulate Recruitment of cDC1 into the Tumor  
1035 Microenvironment Promoting Cancer Immune Control. *Cell* **172**, 1022-  
1036 1037.e14 (2018).
- 1037 55. Savas, P. *et al.* Single-cell profiling of breast cancer T cells reveals a tissue-  
1038 resident memory subset associated with improved prognosis. *Nat. Med.* **24**,  
1039 986–993 (2018).
- 1040 56. Zheng, C. *et al.* Landscape of Infiltrating T Cells in Liver Cancer Revealed by  
1041 Single-Cell Sequencing. *Cell* **169**, 1342-1356.e16 (2017).
- 1042 57. Crinier, A. *et al.* High-Dimensional Single-Cell Analysis Identifies Organ-  
1043 Specific Signatures and Conserved NK Cell Subsets in Humans and Mice.  
1044 *Immunity* **0**, 1–16 (2018).
- 1045 58. André, P. *et al.* Anti-NKG2A mAb Is a Checkpoint Inhibitor that Promotes Anti-  
1046 tumor Immunity by Unleashing Both T and NK Cells. *Cell* **175**, 1731-1743.e13  
1047 (2018).
- 1048 59. van Montfoort, N. *et al.* NKG2A Blockade Potentiates CD8 T Cell Immunity  
1049 Induced by Cancer Vaccines. *Cell* **175**, 1744-1755.e15 (2018).
- 1050 60. Terawaki, S. *et al.* IFN- $\alpha$  Directly Promotes Programmed Cell Death-1  
1051 Transcription and Limits the Duration of T Cell-Mediated Immunity. *J.*  
1052 *Immunol.* **186**, 2772–2779 (2011).
- 1053 61. Ancuta, P. *et al.* Transcriptional profiling reveals developmental relationship  
1054 and distinct biological functions of CD16<sup>+</sup> and CD16<sup>-</sup> monocyte subsets.  
1055 *BMC Genomics* **10**, 403 (2009).

- 1056 62. Rőszer, T. Understanding the Mysterious M2 Macrophage through Activation  
1057 Markers and Effector Mechanisms. *Mediators Inflamm.* **2015**, 1–16 (2015).
- 1058 63. Zagórska, A., Través, P. G., Lew, E. D., Dransfield, I. & Lemke, G.  
1059 Diversification of TAM receptor tyrosine kinase function. *Nat. Immunol.* **15**,  
1060 920–928 (2014).
- 1061 64. Hart, K. M., Bak, S. P., Alonso, A. & Berwin, B. Phenotypic and Functional  
1062 Delineation of Murine CX3CR1+ Monocyte-Derived Cells in Ovarian Cancer.  
1063 *Neoplasia* **11**, 564-IN10 (2009).
- 1064 65. Zheng, J. *et al.* Chemokine receptor CX3CR1 contributes to macrophage  
1065 survival in tumor metastasis. *Mol. Cancer* **12**, 141 (2013).
- 1066 66. Schraufstatter, I. U., Zhao, M., Khaldoyanidi, S. K. & Discipio, R. G. The  
1067 chemokine CCL18 causes maturation of cultured monocytes to macrophages  
1068 in the M2 spectrum. *Immunology* **135**, 287–298 (2012).
- 1069 67. Steen, K. A., Xu, H. & Bernlohr, D. A. FABP4/aP2 Regulates Macrophage  
1070 Redox Signaling and Inflammasome Activation via Control of UCP2. *Mol. Cell.*  
1071 *Biol.* **37**, (2017).
- 1072 68. Pan, C. *et al.* Aldehyde dehydrogenase 2 inhibits inflammatory response and  
1073 regulates atherosclerotic plaque. *Oncotarget* **7**, 35562–35576 (2016).
- 1074 69. Lim, H. Y. *et al.* Hyaluronan Receptor LYVE-1-Expressing Macrophages  
1075 Maintain Arterial Tone through Hyaluronan-Mediated Regulation of Smooth  
1076 Muscle Cell Collagen. *Immunity* **49**, 326-341.e7 (2018).
- 1077 70. Xu, H., Chen, M., Reid, D. M. & Forrester, J. V. LYVE-1–Positive Macrophages  
1078 Are Present in Normal Murine Eyes. *Investig. Ophthalmology Vis. Sci.* **48**, 2162  
1079 (2007).
- 1080 71. Chakarov, S. *et al.* Two distinct interstitial macrophage populations coexist  
1081 across tissues in specific subtissular niches. *Science* **363**, eaau0964 (2019).
- 1082 72. Wu, T. *et al.* Regulating Innate and Adaptive Immunity for Controlling SIV  
1083 Infection by 25-Hydroxycholesterol. *Front. Immunol.* **9**, 2686 (2018).
- 1084 73. Hogan, L. E., Jones, D. C. & Allen, R. L. Expression of the innate immune  
1085 receptor LILRB5 on monocytes is associated with mycobacteria exposure.  
1086 *Sci. Rep.* **6**, 21780 (2016).
- 1087 74. Shojaei, F. *et al.* Bv8 regulates myeloid-cell-dependent tumour angiogenesis.

- 1088 *Nature* **450**, 825–831 (2007).
- 1089 75. van Galen, P. *et al.* Single-Cell RNA-Seq Reveals AML Hierarchies Relevant to  
1090 Disease Progression and Immunity. *Cell* **176**, 1265–1281.e24 (2019).
- 1091 76. Liu, H., Shi, B., Huang, C.-C., Eksarko, P. & Pope, R. M. Transcriptional  
1092 diversity during monocyte to macrophage differentiation. *Immunol. Lett.* **117**,  
1093 70–80 (2008).
- 1094 77. Kelly, L. M. MafB is an inducer of monocytic differentiation. *EMBO J.* **19**,  
1095 1987–1997 (2000).
- 1096 78. Hickey, M. M. *et al.* Hypoxia-inducible factor 2 $\alpha$  regulates macrophage  
1097 function in mouse models of acute and tumor inflammation. *J. Clin. Invest.*  
1098 **120**, 2699–2714 (2010).
- 1099 79. Stoeckius, M. *et al.* Simultaneous epitope and transcriptome measurement in  
1100 single cells. *Nat. Methods* **14**, 865–868 (2017).
- 1101 80. Zhang, A. W. *et al.* Probabilistic cell-type assignment of single-cell RNA-seq  
1102 for tumor microenvironment profiling. *Nat. Methods* **16**, 1007–1015 (2019).
- 1103 81. Newman, A. M. *et al.* Determining cell type abundance and expression from  
1104 bulk tissues with digital cytometry. *Nat. Biotechnol.* **37**, 773–782 (2019).
- 1105 82. Samstein, R. M. *et al.* Tumor mutational load predicts survival after  
1106 immunotherapy across multiple cancer types. *Nat. Genet.* (2019).  
1107 doi:10.1038/s41588-018-0312-8
- 1108 83. Nakanishi, Y., Lu, B., Gerard, C. & Iwasaki, A. CD8<sup>+</sup> T lymphocyte  
1109 mobilization to virus-infected tissue requires CD4<sup>+</sup> T-cell help. *Nature* **462**,  
1110 510–513 (2009).
- 1111 84. Iijima, N. & Iwasaki, A. Access of protective antiviral antibody to neuronal  
1112 tissues requires CD4 T-cell help. *Nature* **533**, 552–556 (2016).
- 1113 85. Quezada, S. A. *et al.* Tumor-reactive CD4<sup>+</sup> T cells develop cytotoxic activity  
1114 and eradicate large established melanoma after transfer into lymphopenic  
1115 hosts. *J. Exp. Med.* **207**, 637–650 (2010).
- 1116 86. Borst, J., Ahrends, T., Bąbala, N., Melief, C. J. M. & Kastenmüller, W. CD4<sup>+</sup> T  
1117 cell help in cancer immunology and immunotherapy. *Nat. Rev. Immunol.* **18**,  
1118 635–647 (2018).
- 1119 87. Van Den Brink, S. C. *et al.* Single-cell sequencing reveals dissociation-

- 1120 induced gene expression in tissue subpopulations. *Nat. Methods* **14**, 935–936  
1121 (2017).
- 1122 88. Buffa, F. M., Harris, A. L., West, C. M. & Miller, C. J. Large meta-analysis of  
1123 multiple cancers reveals a common, compact and highly prognostic hypoxia  
1124 metagene. *Br. J. Cancer* **102**, 428–435 (2010).
- 1125 89. McGinnis, C. S., Murrow, L. M. & Gartner, Z. J. DoubletFinder: Doublet  
1126 Detection in Single-Cell RNA Sequencing Data Using Artificial Nearest  
1127 Neighbors. *Cell Syst.* **8**, 329–337.e4 (2019).
- 1128 90. Wolock, S. L., Lopez, R. & Klein, A. M. Scrublet: Computational Identification  
1129 of Cell Doublets in Single-Cell Transcriptomic Data. *Cell Syst.* **8**, 281–291.e9  
1130 (2019).
- 1131 91. Qiu, X. *et al.* Reversed graph embedding resolves complex single-cell  
1132 trajectories. *Nat. Methods* **14**, 979–982 (2017).
- 1133 92. Street, K. *et al.* Slingshot: Cell lineage and pseudotime inference for single-  
1134 cell transcriptomics. *BMC Genomics* **19**, 1–16 (2018).
- 1135 93. Cannoodt, R. *et al.* SCORPIUS improves trajectory inference and identifies  
1136 novel modules in dendritic cell development. *bioRxiv* 1–15 (2016).  
1137 doi:10.1101/079509
- 1138 94. Gaude, E. & Frezza, C. Tissue-specific and convergent metabolic  
1139 transformation of cancer correlates with metastatic potential and patient  
1140 survival. *Nat. Commun.* **7**, 1–9 (2016).
- 1141 95. Federico, A. & Monti, S. hypeR: an R package for geneset enrichment  
1142 workflows. *Bioinformatics* **36**, 1307–1308 (2019).
- 1143 96. Bosisio, F. M. *et al.* Functional heterogeneity of lymphocytic patterns in  
1144 primary melanoma dissected through single-cell multiplexing. *Elife* **9**, 1–21  
1145 (2020).
- 1146 97. Boeckx, B. *et al.* The genomic landscape of nonsmall cell lung carcinoma in  
1147 never smokers. *Int. J. cancer* ijc.32797 (2019). doi:10.1002/ijc.32797
- 1148 98. Davie, K. *et al.* A Single-Cell Transcriptome Atlas of the Aging *Drosophila*  
1149 Brain. *Cell* **174**, 982–998.e20 (2018).
- 1150 99. Wernersson, S. & Pejler, G. Mast cell secretory granules: Armed for battle.  
1151 *Nat. Rev. Immunol.* **14**, 478–494 (2014).

- 1152 100. Qi, X. *et al.* Antagonistic Regulation by the Transcription Factors C/EBP $\alpha$  and  
1153 MITF Specifies Basophil and Mast Cell Fates. *Immunity* **39**, 97–110 (2013).  
1154  
1155

## 1156 Legends to Figures

### 1157 Fig. 1. Experimental design and cell typing

1158 **a** Analysis workflow of tumour and matched normal samples from 3 cancer types. **b-d** t-  
1159 SNE representation for LC (n=93,576 cells), CRC (n=44,685) and OvC (45,115) colour-  
1160 coded for cell type (**b**), sample origin (**c**) and patient (**d**). **e** Bar plots representing per cell  
1161 type from left to right: the fraction of cells per tissue and per origin, the number of cells,  
1162 the total number of transcripts. Dendritic cells were transcriptionally most active ( $p <$   
1163  $1.6 \times 10^{-10}$ ). **f** Fraction of cells for major cell types per cancer type. T-cells were most  
1164 frequent in LC ( $p < 0.0047$ ).

### 1165 Fig. 2. Clustering 8,223 ECs

1166 **a** t-SNEs colour-coded for annotated ECs by unaligned and CCA aligned clustering. **b** t-  
1167 SNEs with EC marker gene expression for CCA clusters. **c** Marker gene expression per  
1168 EC cluster. **d** Fraction of cells in each cancer type per EC cluster. **e** Fraction of EC clusters  
1169 per cancer type (left) and sample origin (right). **f** Normal/tumour ratio of relative % of EC  
1170 clusters,  $<1$  indicates tumour enrichment. Tip ECs ( $FDR=1.4 \times 10^{-141}$ ) and HEVs  
1171 ( $FDR=2.3 \times 10^{-60}$ ) were enriched in tumour. **g** t-SNEs of cEC clusters by unaligned  
1172 clustering, colour-coded by cluster, sample origin and cancer type, including a zoom-in  
1173 of the NEC4 cluster (right). **h** t-SNE of marker gene expression in cEC clusters. **i-k**  
1174 Heatmap of differentially expressed genes in cEC clusters (**i**), of TF activity by SCENIC for  
1175 EC (**j**) or cEC clusters (**k**). **l,m** Heatmap showing metabolic activity for EC (**l**) or cEC clusters  
1176 (**m**).

### 1177 Fig. 3. Characterization of 24,622 fibroblasts

1178 **a** t-SNE colour-coded for annotated fibroblasts by unaligned clustering. **b** t-SNEs with  
1179 marker gene expression in unaligned clusters. **c** t-SNE colour-coded for annotated  
1180 fibroblasts by CCA. **d** t-SNE with marker gene expression in CCA clusters. **e** Fraction of  
1181 fibroblast clusters per cancer type (left) and sample origin (right). C7-C11s are shared by  
1182 CRC, LC and OvC. **f,g** Heatmap of marker gene expression (**f**) and functional gene sets  
1183 (**g**). **h** Normal/tumour ratio of relative % of fibroblast clusters,  $<1$  indicates tumour  
1184 enrichment. Pericytes were enriched in tumour ( $FDR=7.8 \times 10^{-10}$ ). **i,j** Heatmap of TF activity  
1185 (**i**) or metabolic activity (**j**) in fibroblast clusters.



1186 **Fig. 4. Clustering 2,722 DCs**

1187 **a** t-SNEs colour-coded for annotated DCs by unaligned and CCA aligned clustering. **b** t-  
1188 SNEs with DC marker gene expression in CCA aligned clusters. **c** Heatmap for differential  
1189 gene expression in unaligned clusters. **d** Fraction of DC clusters per cancer type (left) and  
1190 sample origin (right). Migratory cDCs were depleted in OvC (FDR=0.017). **e** Fraction of  
1191 cells in each cancer type per cluster. **f** t-SNEs with gene expression (upper) and  
1192 corresponding TF activity (lower). **g** Heatmap showing TF activity in CCA aligned clusters.  
1193 **h** Trajectory inference analysis of cDC-related subclusters. **i** Marker gene expression  
1194 along the cDC trajectory. **j,k** Marker gene expression (**j**) and expression dynamics (**k**)  
1195 during cDC maturation. **l** TF activation dynamics of cDC2 to migratory cDC differentiation.

1196 **Fig. 5. B-cell taxonomy and developmental trajectory**

1197 **a** t-SNEs colour-coded for annotated B-cells using unaligned and CCA aligned clustering.  
1198 **b** t-SNEs with marker gene expression in CCA clusters. **c** Heatmap of functional gene  
1199 sets in CCA clusters. **d** Fraction of B-cell clusters per cancer type (left) and sample origin  
1200 (right). **e** Fraction of cells in each cancer type per cluster. **f** Heatmap with TF activity by  
1201 SCENIC, for follicular B-cell (left) or plasma cell clusters (right). **g** Developmental trajectory  
1202 for GC-dependent memory B-cells, colour-coded by cell type (left) and pseudotime (right).  
1203 **h** Marker gene expression of the GC-memory B-cell trajectory as in (**g**). **i** Trajectory of IgM<sup>-</sup>  
1204 memory B to IgG<sup>+</sup> or IgA<sup>+</sup> plasma cells, colour-coded by branch type (left) and pseudotime  
1205 (right). **j** Marker gene expression dynamics during plasma cell differentiation as in (**i**).

1206 **Fig. 6. Profiling 52,494 T-/NK-cells**

1207 **a** t-SNEs colour-coded for annotated T-/NK-cell using unaligned and CCA aligned  
1208 clustering. **b** t-SNEs with marker gene expression in CCA clusters. **c** Heatmap of  
1209 functional gene sets in CCA clusters. **d** Fraction of cells for T-/NK-cell clusters per cancer  
1210 type (left) and sample origin (right). **e** Normal/tumour ratio of relative % of T-/NK-cell  
1211 clusters, <1 indicates tumour enrichment. C1, C2, C5, C7, C8 were enriched in tumour  
1212 (FDR<5.1x10<sup>-25</sup>), C9 was enriched in normal (FDR=1.5x10<sup>-219</sup>). **f** Fraction of T-/NK-cells in  
1213 each cancer type per cluster. C4 and C8 were rare in CRC (FDR=0.019) and OvC  
1214 (FDR=0.034), respectively. **g** Heatmap with TF activity of T-/NK-cell clusters by SCENIC.  
1215 **h** Differentiation trajectory for CD8<sup>+</sup> T cell lineages, colour-coded by cell type (left) and

1216 pseudotime (right). **i** Density plots for CRC, LC and OvC along the two CD8<sup>+</sup> T-cell  
1217 trajectories.

### 1218 **Fig. 7. Profiling of monocytes, macrophages and neutrophils**

1219 **a** t-SNE colour-coded for annotated myeloid cell using unaligned clustering. **b** t-SNEs  
1220 with marker gene expression in myeloid clusters. **c** Heatmap of functional gene sets in  
1221 myeloid clusters. **d** Fraction of myeloid clusters per cancer type (left) and sample origin  
1222 (right). C9 was enriched in normal (FDR=3.0x10<sup>-31</sup>) and C8 in normal lung (FDR ≈ 0) tissue.  
1223 C5-C7 and C10 (FDR < 3.3x10<sup>-31</sup>) were enriched in tumour. **e** Fraction of cells in each  
1224 cancer type per cluster. **f** Monocyte-to-macrophage differentiation trajectory, colour-  
1225 coded by cluster (left) or pseudotime (right). **g,h** Gene expression dynamics during  
1226 differentiation of C1 monocytes to C4 macrophages (**g**), or terminal differentiation of  
1227 C5/C7 macrophages (**h**). **i** Heatmap showing TF activity by SCENIC. **j** TF activation (left)  
1228 or inactivation (right) during monocyte-to-macrophage differentiation, before branching  
1229 into terminal differentiation.

### 1230 **Fig. 8. Validation of the stromal blueprint**

1231 **a** t-SNE of BC cells colour-coded for cell types. **b** t-SNEs of T-/NK-cells by unaligned  
1232 clustering or CCA-aligned clustering with 3'-scRNA-seq data. **c** t-SNEs of CCA-aligned  
1233 clusters colour-coded for annotated DCs (upper) and cancer type (lower). **d** Heatmap of  
1234 marker gene expression across DC clusters in different cancer types. **e** TF activity across  
1235 DC subclusters in different cancer types. **f** Fraction of T-/NK-cell clusters in pre-treatment  
1236 biopsies from melanoma patients treated with ICI. **g** Violin plot showing *TCF7* expression  
1237 in T-/NK-cell clusters from pre-treatment melanoma patients. **h** Receiver operating  
1238 characteristic (ROC) analysis to evaluate the predictive effect of naïve CD4<sup>+</sup> T-cells on  
1239 response to checkpoint immunotherapy. The area under the ROC curve (AUC) was used  
1240 to quantify response prediction.

### 1241 **Fig. 9 Validation of the stromal blueprint by CITE-seq**

1242 **a** t-SNEs of CITE-seq profiled BC cells clustered into cell types based on RNA (left) or  
1243 protein (right) data. **b** Marker gene or protein expression for each cell type. **c** t-SNE plots  
1244 showing BC T-/NK-cells co-clustered with 3'-scRNA-seq data from other cancer types  
1245 (left), while highlighting only T-/NK-cells with BC origin (right). **d** Heatmap with marker

1246 gene expression of T-/NK-cell clusters. **e** Expression by CITE-seq markers per T-/NK-cell  
1247 cluster.  
1248

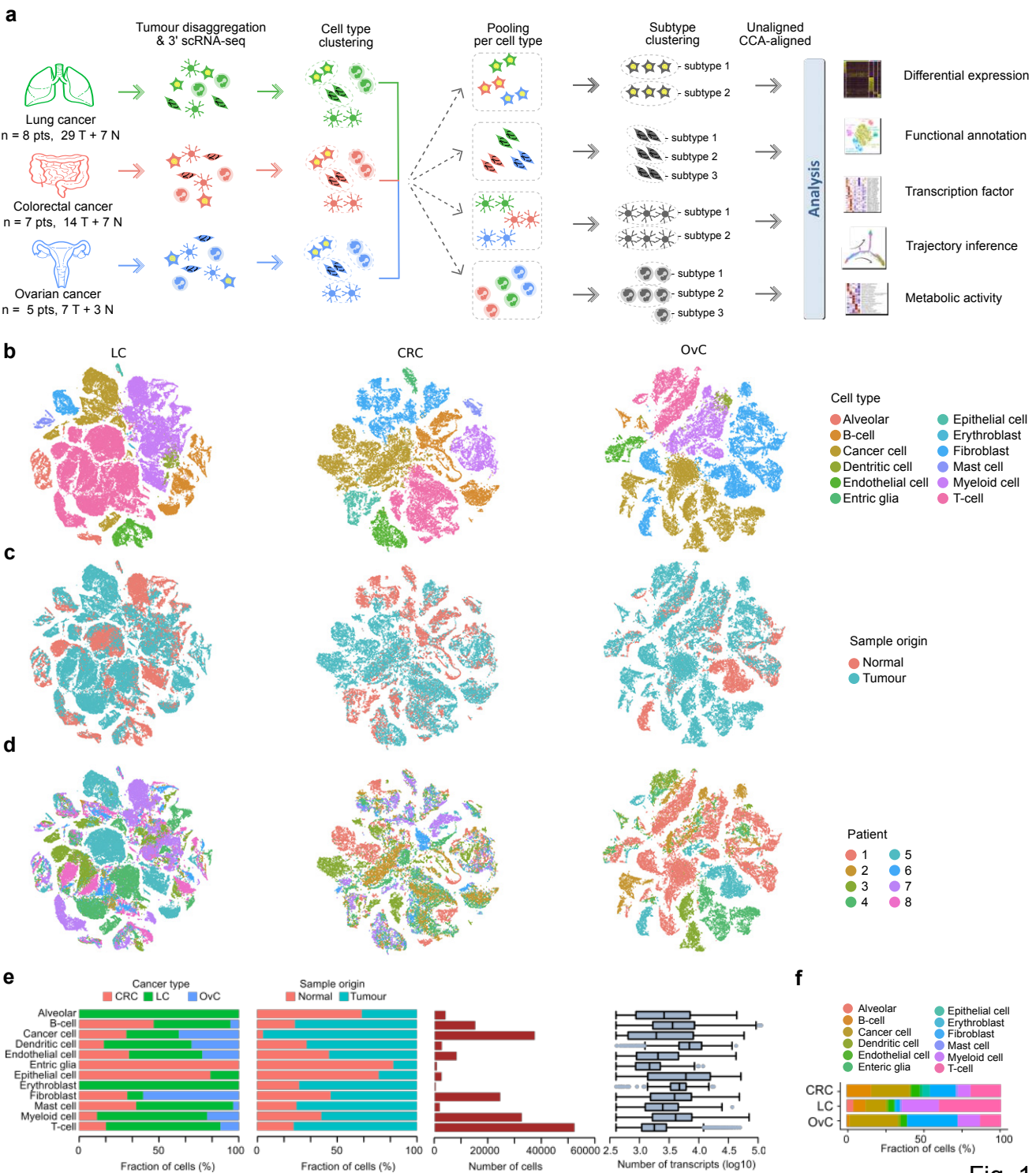


Fig. 1

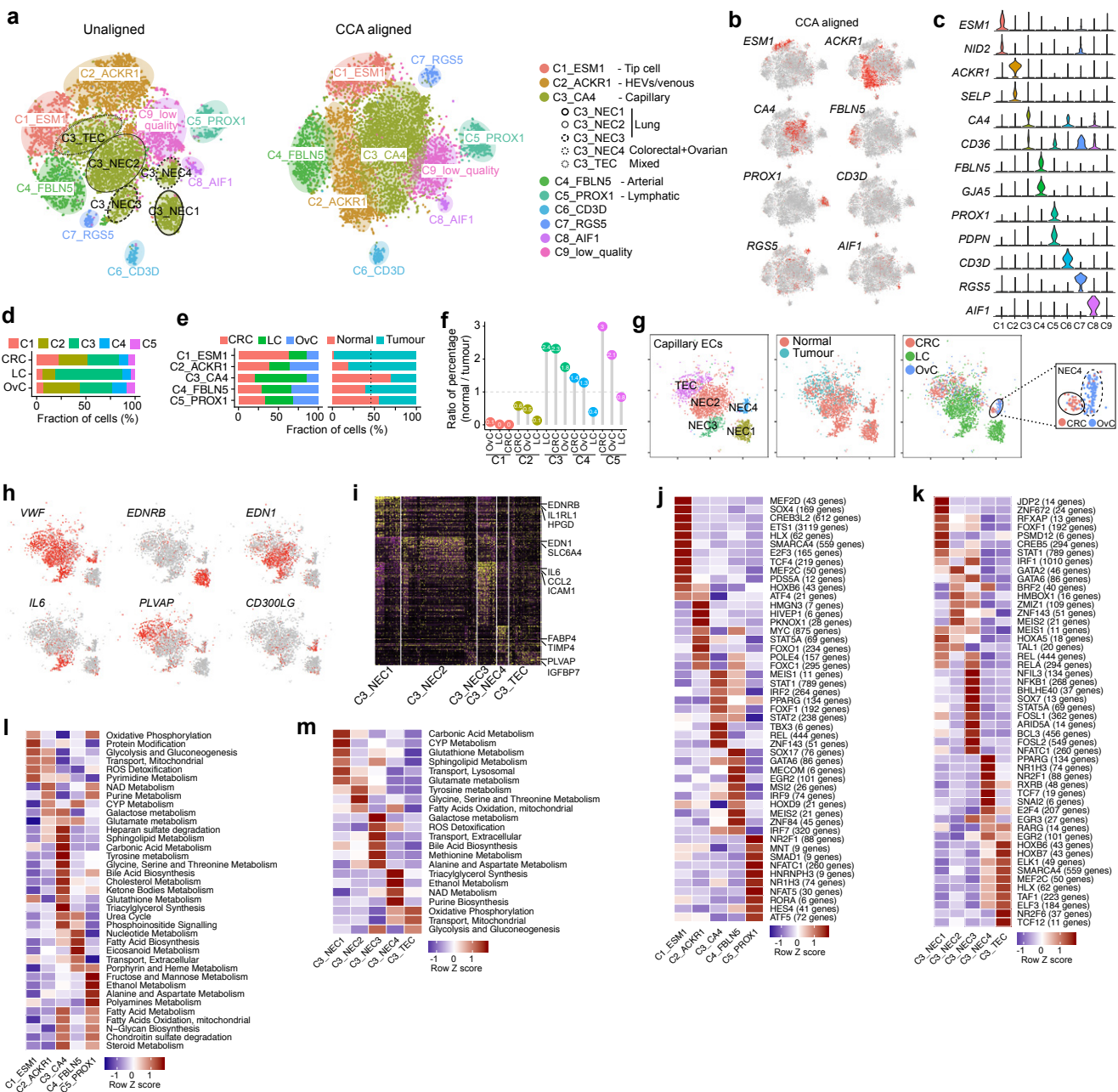
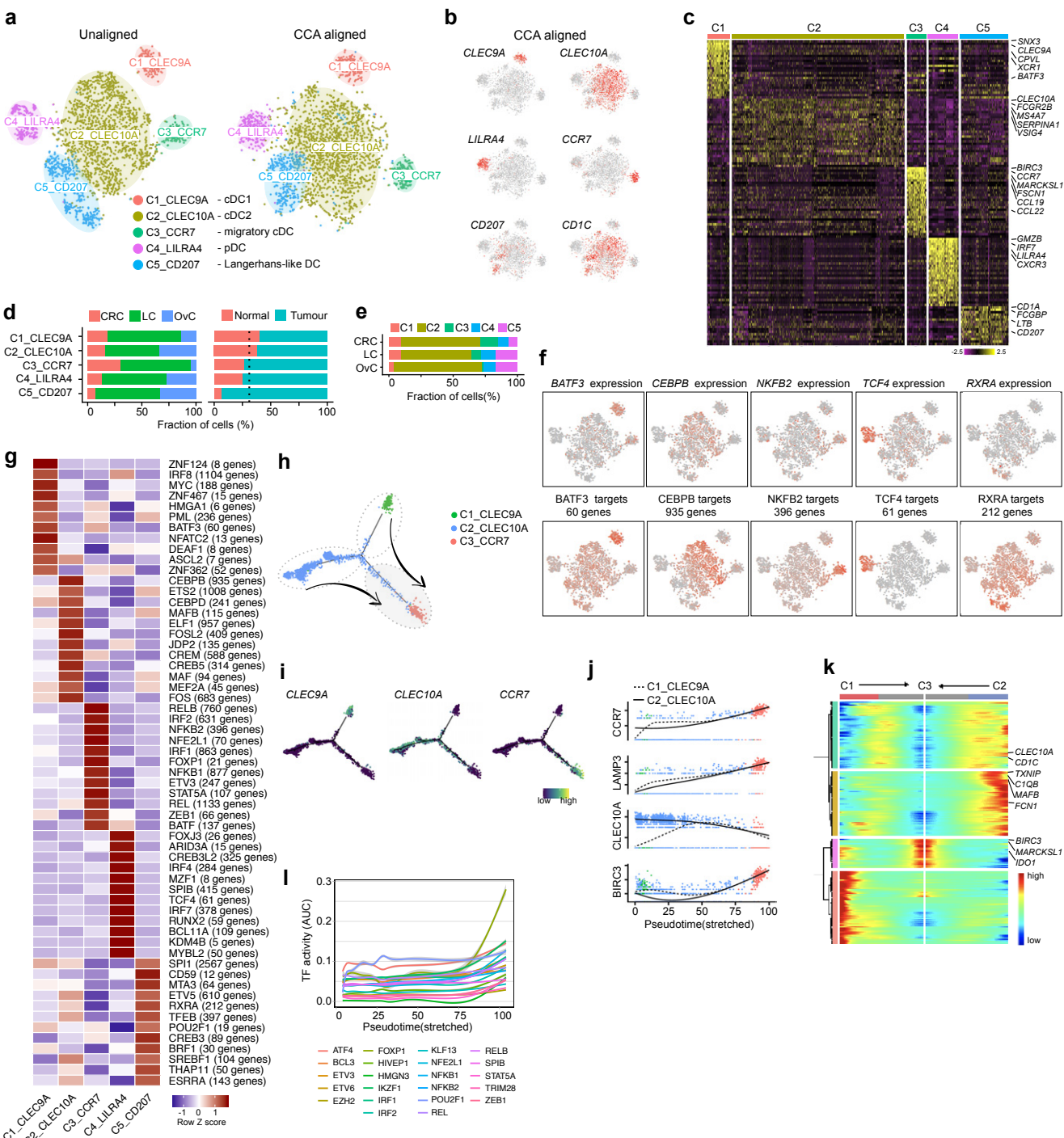


Fig. 2



Fig. 3



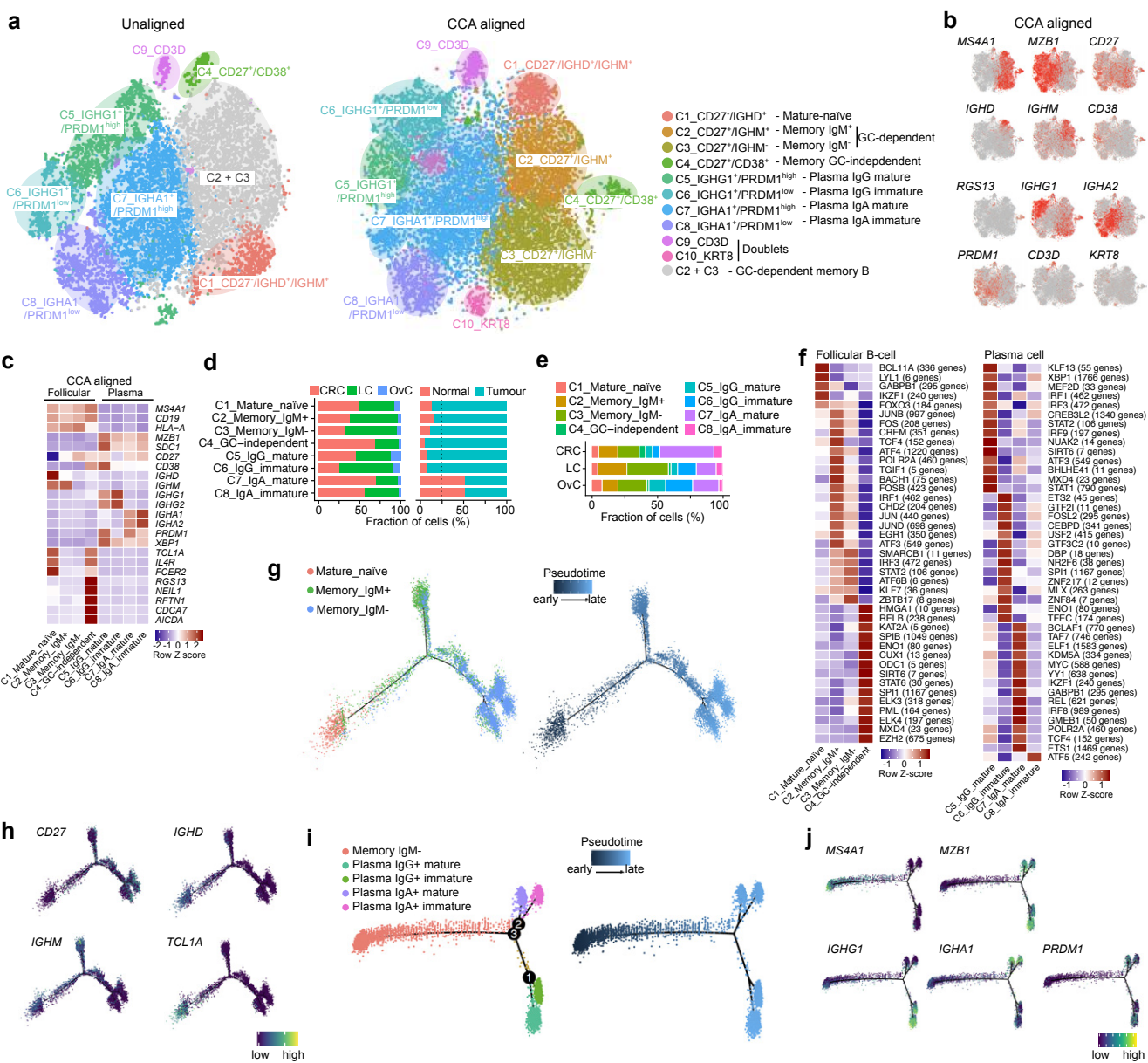
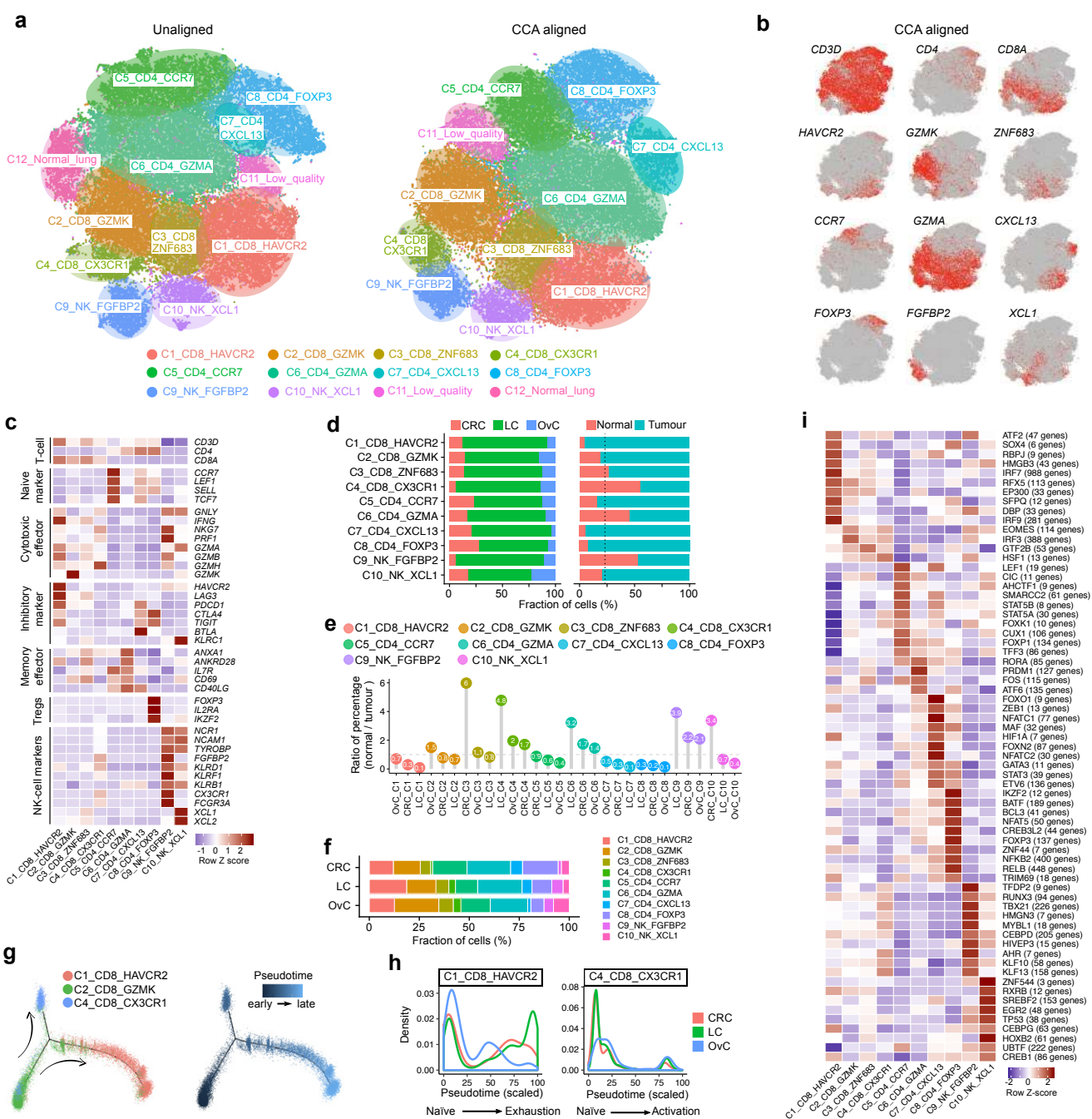
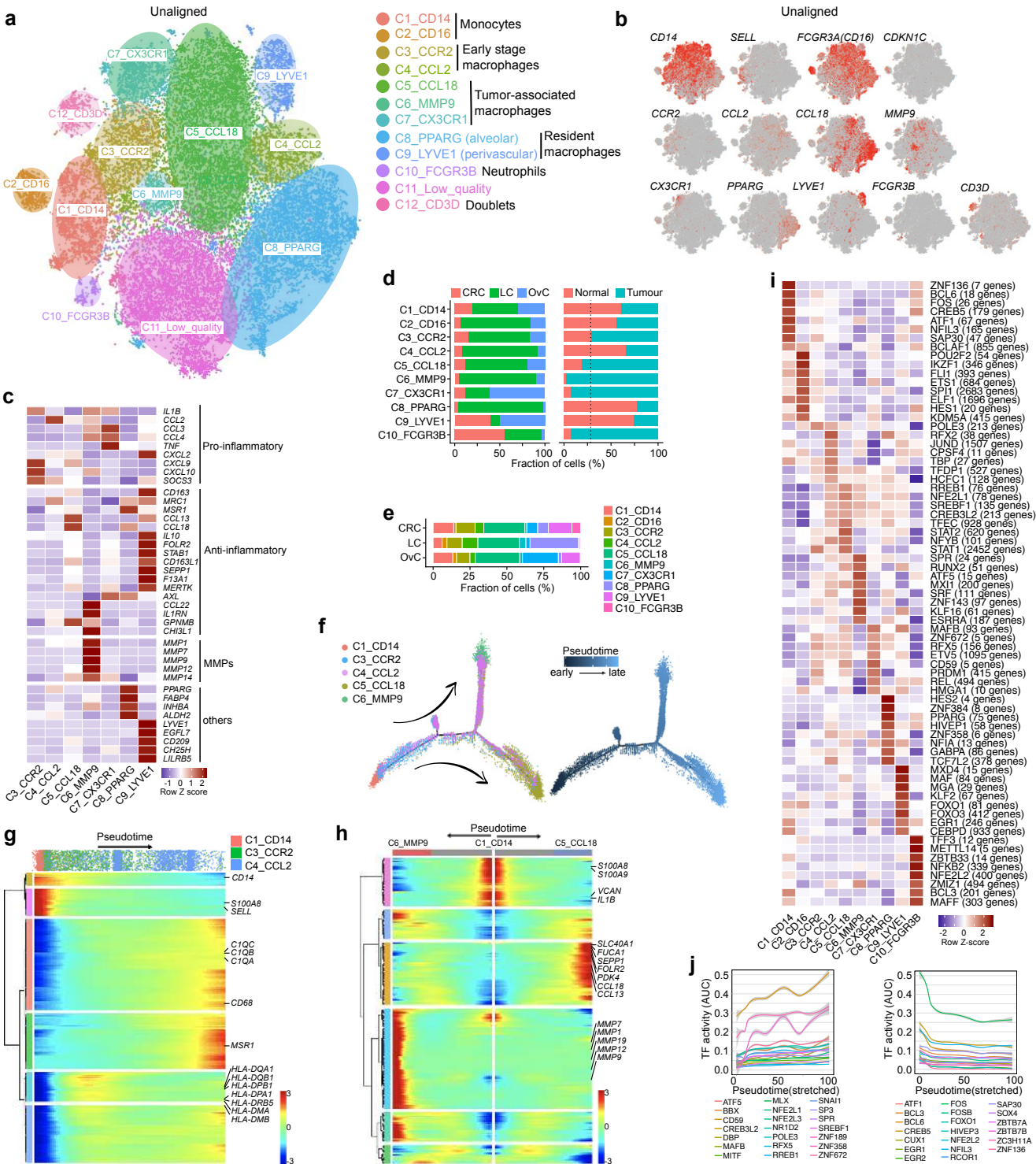


Fig. 5







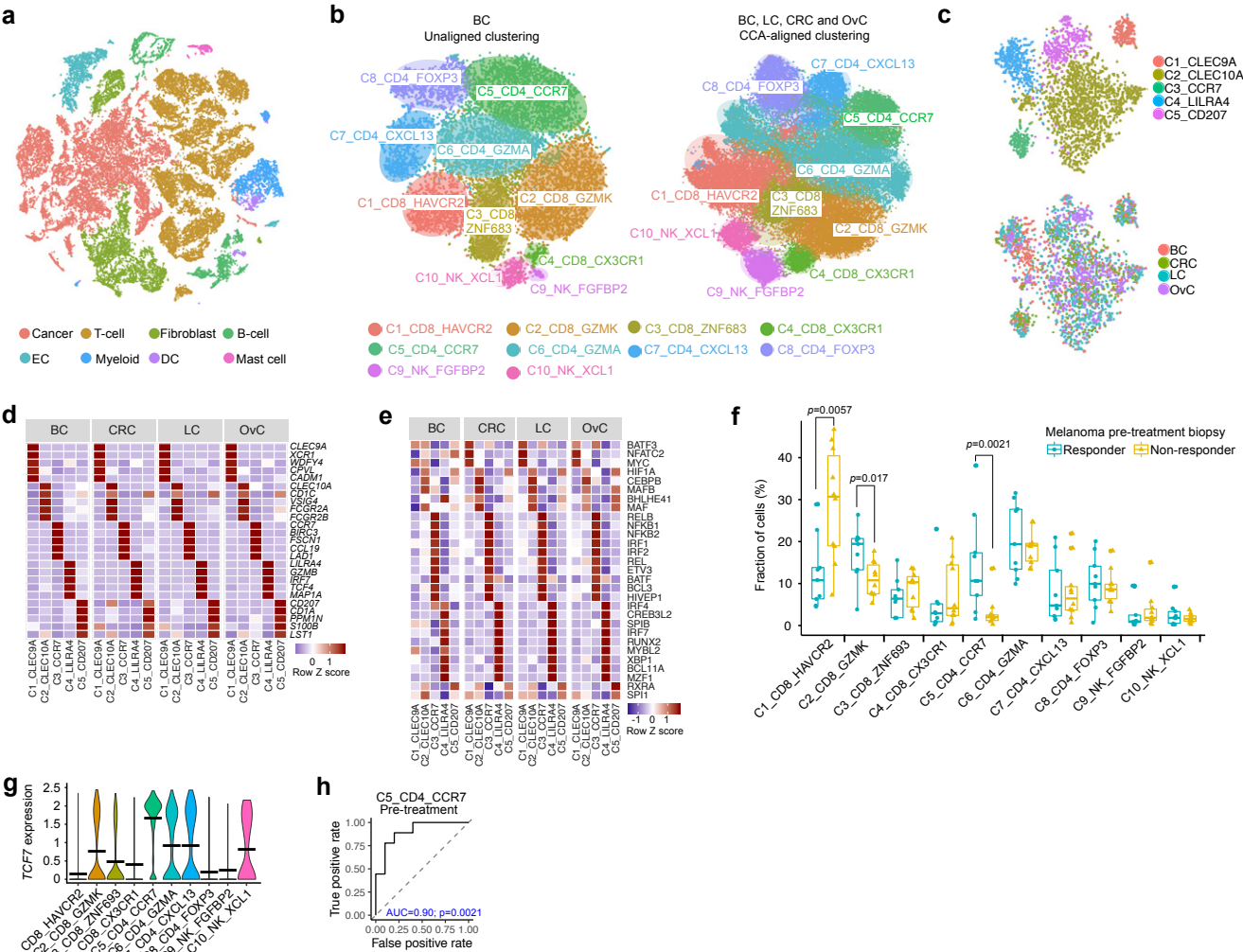


Fig. 8

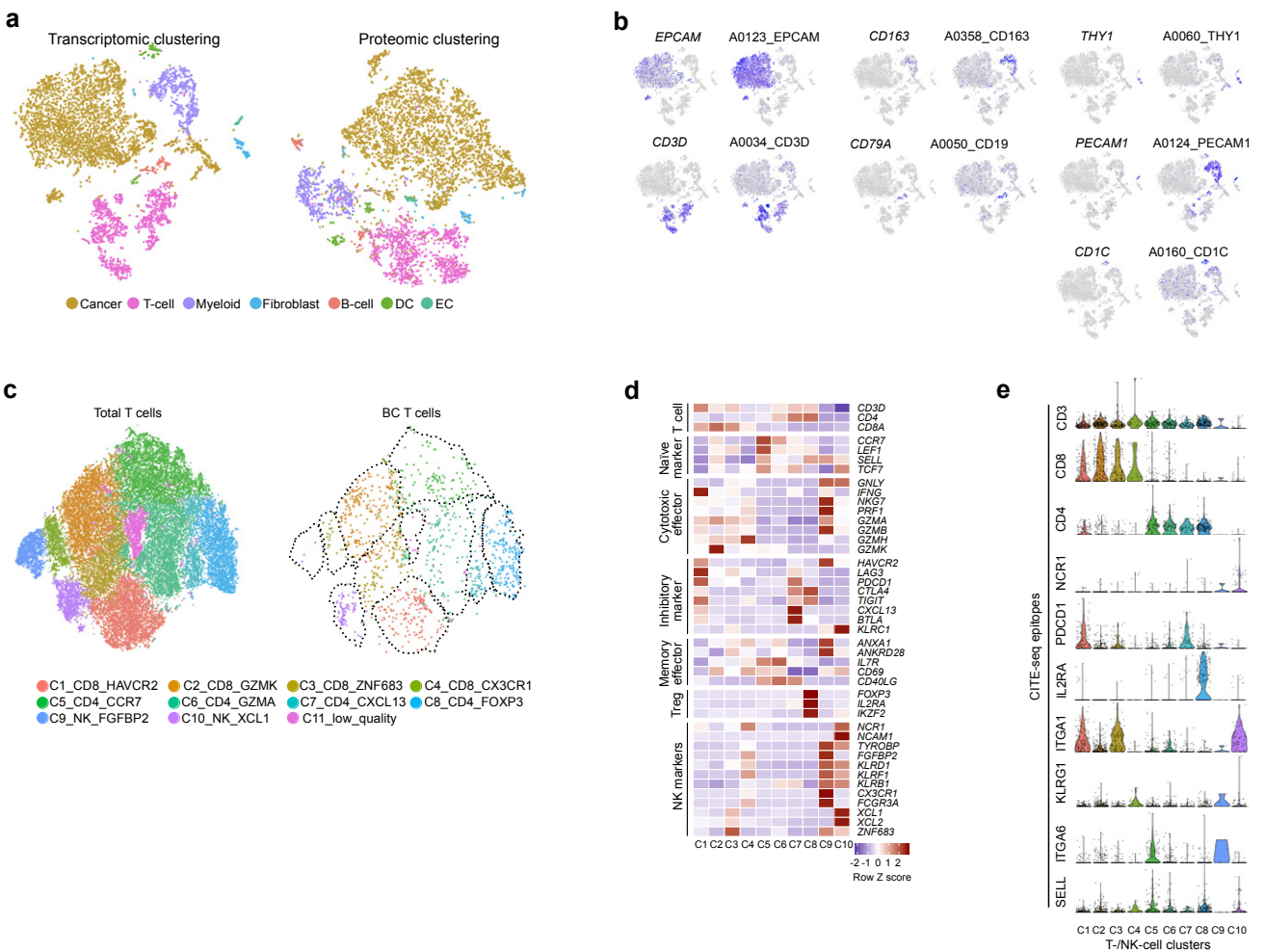


Fig. 9